Organic Small Molecules with Tunable π-π Stacking as Dopant-Free Hole Transport Materials for High-Performance Perovskite Solar Cells

Zhiwen Zhou[1], Qisheng Wu[2], Rui Cheng[1], Hong Zhang[3], Sijia Wang[1], Mojun Chen[1], Maohai Xie[4], Paddy Kwok Leung Chan[1], Michael Grätzel[3*] and Shien-Ping Feng[1*]*

[1]Department of Mechanical Engineering, The University of Hong Kong, Pokfulam Road, Hong Kong, PR China.

[2] Department of Chemical Engineering and Materials Science, Michigan State University, East Lansing, Michigan 48824, United States.

[3] Laboratory of Photonics and Interfaces, Institute of Chemical Sciences and Engineering, École Polytechnique Fédérale de Lausanne Station 6, CH-1015 Lausanne, Switzerland

[4] Department of Physics, The University of Hong Kong, Pokfulam Road, Hong Kong, PR China.

Correspondence and requests for materials should be addressed to Prof. S. P. Feng (hpfeng@hku.hk) , Prof. Michael Grätzel (michael.graetzel@epfl.ch) or Prof. P. K. L. Chan (email: pklc@hku.hk)

Abstract:

Crystallized p-type small-molecule semiconductors have great potential as efficient and stable hole transporting materials (HTMs) for perovskite solar cells (PSCs) due to their relatively high hole mobility, good stability and tunable HOMOs depending on the molecular orientation. Here, a thienoacene-based organic semiconductor, 2,9-diphenyldinaphtho[2,3-b:2',3'-f]thieno[3,2-b]thiophene (DPh-DNTT), was thermally evaporated and employed as the dopant-free HTM that can be scaled up for large-area fabrication. By controlling the deposition temperature, the molecular orientation was modulated into a dominated face-on orientation possessing π-π stacking direction

towards the surface normal to maximize the out-of-plane carrier mobility. With an engineered face-on orientation, the DPh-DNTT film shows an improved out-of-plane mobility of 3.3 $\times 10^{-2}$ $cm^2V^{-1}s^{-1}$, outperforming the HTMs reported so far. Such orientation-reinforced mobility contributes to a remarkable efficiency of 20.2% for $CH_3NH_3PbI_3$ inverted PSCs with enhanced stability. The results reported here provide insights into engineering the orientation of molecules for the dopant-free organic HTMs for PSCs.

Keywords: dopant-free, hole transport materials (HTM), mobility, molecular orientation, $MAPbI_3$ solar cells

Introduction

Organic-inorganic hybrid perovskite solar cells (PSCs) have attracted tremendous attention owing to their excellent photoelectric properties such as high light absorption,[1] superior carrier diffusion length,[2] low non-radiative recombination[3] and especially their proud power conversion efficiencies (PCE).[4-8] To commercialize the PSCs, great efforts have been made to promote the PCE as well as long-term stability by means of solvent engineering, additive engineering and composition engineering.[9-12] Hole transporting materials (HTMs) play a crucial role in the electrical performance and shelf-life stability of PSC devices.[13] During the past decade, the PCE has increased from 3.8% to more than 25% based on the conventionally used HTMs of 2,2',7,7'-tetrakis(N,N-di-*p*-methoxyphenylamine)-9,9'-spirobifluorene (spiro-OMeTAD) or poly(triarylamine) (PTAA).[1,8,14] However, these two effective HTMs are still suffering

from high cost, easy degradation and low purity, limiting their applications for the low-cost and large-scale manufacturing of PSCs.[15] In addition, to achieve a sufficient hole conductivity, both molecular spiro-OMeTAD and polymeric PTAA usually require additive dopants including 4-*tert*-butylpyridine (*t*-BP), lithium bis(trifluoromethanesulfonyl)imide (Li-TFSI) and/or the cobalt complex (FK209).[16] Although the hole conductivity has been improved, these hygroscopic and unstable dopants not only cause reproducibility and stability dilemmas but also increase device fabrication complexity.[16] In this regard, developing stable dopant-free HTMs is highly required to ensure the commercialization and mass production of efficient and durable PSCs.

Dopant-free HTMs can be categorized into three main subgroups: inorganic HTMs, polymeric HTMs and organic small-molecule HTMs. Inorganic HTMs generally provide robust device stability, but the attainable efficiency is limited by their relatively poor film quality and severe interfacial charge recombination due to the numerous surface defects.[17] In contrast, their organic counterparts, polymer and small-molecule HTMs, have greater potential to achieve attractive efficiency as well as excellent long-term stability in their pristine form thanks to the high mobility, good stability and considerable hydrophobicity. Furthermore, thiophene-based organic HTMs have been proved to be efficient non-doped HTMs for PSCs due to the large π-conjugation across molecules.[18-19] Meanwhile, the sulfur (S) atoms in thiophene moiety might also induce strong interfacial interactions between HTM and perovskite layer.[20-21] For example, undoped poly(3-hexythiophene) (P_3HT) polymer was utilized as the HTM for PSCs to

achieve a benchmark PCE of 22.7%, of which only 5% efficiency loss was observed after continuous light illumination for over 1300 hours.[22] Nevertheless, P_3HT here required an ultrathin wide-bandgap perovskite as the interlayer to enhance interfacial charge transport, which complicated the device fabrication process and reduced the feasibility. Moreover, it is challenging to use polymeric HTMs in real production due to their inherent polydispersity, low purity, and poor reproducibility.

Different from polymeric HTMs, small-molecule HTMs have well-defined structures, determined molecular weight, synthetic variety and particularly high purity and yield, making them potentially cost-effective HTMs for PSCs.[23-24] Given these merits, abundant emerging small-molecule HTMs have been developed to replace spiro-OMeTAD or PTAA, whereas most of them still require certain doping levels to work efficiently. Despite tremendous efforts to synthesize new small-molecule HTMs, the highest efficiency reported so far is still around 19% for $MAPbI_3$-based solar cells without any additive dopants.[13,25-27] Compared with the giant research enthusiasm on broadening the library of HTMs, little attention has been paid to further exploiting the full potential of existing p-type semiconducting compounds for their efficient utilization as undoped HTMs. In fact, a large number of advanced and cost-effective small-molecule semiconductors have been developed in the field of organic field-effect transistors (OFETs), showing good thermal stability, versatile processability and tunable properties.[23-24] A benchmarked organic semiconductor in OFETs, 6,13-bis(triisopropylsilylethynyl) pentacene (TIPS-pentacene), has been attempted as dopant-free HTMs for PSCs, but a very poor PCE (~12%) was measured.[28] This

inferior PCE could be ascribed to the inherent anisotropic charge transport of organic crystalline semiconductors, caused by the molecular orientations.[29] The charge transport direction is different between OFETs with horizontal channels and layered PSCs with top-bottom electrodes. Therefore, small-molecule semiconductors even with outstanding field-effect mobility may not be used as HTMs to obtain high-performance PSC devices. In addition to the general optimization of film thickness, the molecular-orientation adjustment of small-molecule semiconductors should be considered for achieving superior performance of PSCs based on these semiconductors as undoped HTMs.

In this work, we demonstrated the thienoacene-based organic semiconductor, namely 2,9-diphenyldinaphtho[2,3-b:2',3'-f]thieno[3,2-b]thiophene (DPh-DNTT) as an effective HTM without any dopants in inverted planar PSCs. To enhance the out-of-plane hole mobility, the molecular orientation was modulated to a face-on orientation with strong π-π interactions along the substrate normal, which was realized by studying the substrate-temperature effect on molecular orientations during the thermal evaporation process. Specifically, with engineered face-on orientations at lower temperature, the DPh-DNTT film showed five times enhanced intrinsic hole mobility of 3.3 $\times 10^{-2}$ $cm^2V^{-1}s^{-1}$ along the out-of-plane direction. This orientation-reinforced mobility was much higher than that of the doped spiro-OMeTAD ($\sim 10^{-4}$ $cm^2V^{-1}s^{-1}$)[21] and thus resulted in a remarkable PCE of 20.2% for $MAPbI_3$-based PSCs. Our device also exhibited negligible hysteresis and superior long-term stability, retaining 90% of its intrinsic efficiency after a 45-day exposure to ambient with a relative humidity of

60% ± 10% in dark. This excellent ambient stability attributes to the hydrophobicity of DPh-DNTT and the strong S-Pb coordination between the DPh-DNTT and perovskite layer. These results offer an orientation engineering strategy for systematic performance optimization of organic HTMs used in PSCs.

Results and discussion

Among the numerous materials developed for OFETs, dinaptho[2,3-*b*:2',3'-*f*]thieno[3,2-b]thiophene (DNTT) and its derivatives (such as alkylated derivative C_{10}-DNTT and phenylated derivative DPh-DNTT) have become promising transistor semiconductors due to their high mobility and good ambient stability.[30-31] The molecular structures of the core DNTT and its derivatives are shown in **Figure 1**a. The core DNTT is rigidly planar π-conjugated structure formed by fusing thiophenes and diacene-rings, which contributes to effective intermolecular orbital overlap in the solid state.[24] The DPh-DNTT derivative is almost linear in molecular shape, however, C_{10}-DNTT molecule shows a zig-zag shape as the molecule shape is less sensitive to the phenyl substituent compared to the alkyl one. It has been revealed that the parent DNTT and its derivatives mentioned above exhibit a typical herringbone stacking mode regardless of the substitutions.[30,32] Such a herringbone packing structure facilitates the formation of two-dimensional charge transport pathways for carriers, leading to excellent high carrier mobility. Considering that the major role of HTMs is extracting holes, the excellent hole mobility of DNTT and its derivatives is the basis for their usage as efficient HTMs for PSCs. On the other hand, tuning a proper molecular orientation is critical to obtain an optimal charge transport efficiency for different

electronic devices based on π-conjugated organic compounds. In OFETs, the formed conductive channel is parallel with the surface of substrates (**Figure 1**b), so the favored molecular orientation with respect to the substrate surface is edge-on or chain-on (**Figure 1**d and f), in which the aligned π-π stacking are largely beneficial to the in-plane carrier transport under the lateral electrical field induced by the source-drain electrodes. Therefore, the reported high-performance OFETs based on DNTT and its derivatives basically showed chain-on orientations with their long backbones perpendicular to the substrates.[23-24] However, in contrast to the transistors, the face-on molecular orientation is preferable for photovoltaic devices inclusive of OPVs and PSCs, to achieve a sufficient hole extraction in the out-of-plane direction (**Figure 1**c and e). Here, we carefully control the deposition temperature to less than 30 °C to ensure the molecular orientation of DPh-DNTT from the commonly reported chain-on mode to the face-on mode and used it as dopant-free HTMs for PSCs. The thermal stability of HTMs is another important concern during the fabrication of PSCs as the crystallization of perovskite layers requires a mild thermal treatment (100 ~ 150 °C).[33] Among the parent DNTT and the two derivatives, DPh-DNTT has the excellent thermal stability and maintains its outstanding performance even at 250 °C, making it promising as the HTM in PSCs.[32] In comparison, the devices based on DNTT or C_{10}-DNTT material cannot hold their original high performances after a mild thermal treatment (~150 °C).[32-34] In the following, we therefore performed a systematic study based on DPh-DNTT semiconductors and demonstrated the excellent performance of PSCs

using the pristine DPh-DNTT as HTMs. Some relevant discussions about DNTT and C_{10}-DNTT will also be provided.

In order to implement DPh-DNTT as a dopant-free HTM and obtain a high PCE, the molecular orientation needed to be turned from the commonly favored chain-on orientation to the rarely reported face-on orientation. Here the modulation of the molecular orientation is partially realized by varying the substrate temperature during the evaporation process. The thermally evaporated DPh-DNTT films are deposited directly on the ITO (indium tin oxide) substrates with an optimized thickness of 30 nm. As illustrated in **Figure 2**, an obvious surface morphology change was observed from the scanning electron microscope (SEM) images under different temperatures, which is further characterized by atomic force microscopy (AFM). Usually a terrace-like surface with large grain sizes is obtained under a higher deposition temperature (160 °C, HT, **Figure 2**a and i), which is comparable with the previous report in OFETs.[35] When the temperature was lowered to the room temperature (25 °C, RT, **Figure 2**d), smoother DPh-DNTT films could be obtained and their nanoscale crystal structures were later shown to improve surface wettability, resulting in the homogeneous growth of top perovskite layers. In addition to the observed morphological changes, the associated molecular orientation of these evaporated DPh-DNTT films was also characterized by the grazing-incidence wide-angle X-ray scattering (GIWAXS) technique, as shown in **Figure 2**e-h. For simplicity, the DPh-DNTT film fabricated at a substrate temperature of 160 °C (HT) will be referred to as HT-DPh, while the RT-DPh indicates that the film was fabricated at room temperature (25 °C, RT). From the GIWAXS pattern of HT-

DPh films, a series of vivid diffraction signals in the out-of-plane direction are indexed as (*00l*) peaks and the intensive reflection arcs in the in-plane direction are correlated with the crystallographic *a-b* units. These signals indicated that in evaporated HT-DPh films, a chain-on molecular orientation alignment accompanied by a crystallographic c-axis almost perpendicular to the substrate surface is dominant, so that high-performance OFETs using DPh-DNTT are typically achieved by heating the substrate.[32] When the substrate temperature is lowered, the brightness of the (001) peak is severely diminished and additional diffraction signals such as (011), (020) and (021) peaks which were previously presented in the in-plane direction of the HT-DPh film, can be clearly identified in the out-of-plane direction of the RT-DPh film. On the other hand, for RT-DPh films, the row of diffraction spots of (*00l*) planes appeared simultaneously along the in-plane direction. These changes in the diffraction signal imply that the molecular orientation of DPh-DNTT crystals can be adjusted, depending on the temperature of the substrate and the preferred molecular orientation in the RT-DPh film is the face-on orientation.

As mentioned earlier, the charge transport capability of an organic semiconductor is largely dependent on the orientation of the molecular arrangement. As a result, we further characterized the carrier transport anisotropy by measuring the carrier mobility along the in-plane and out-of-plane directions via OFET devices and hole-only devices with the structure of ITO/NiO_x/DPh-DNTT/Au, respectively. As shown in the transfer curves of **Figure S**1, OFETs with HT-DPh active layers exhibited excellent electrical performances with an averaged field-effect mobility ($\mu_{//}$) of 4.64 $cm^2/V^{-1}s^{-1}$, which is

consistent with the reported value of evaporated HT-DPh films showing a favorable chain-on orientation.[35] This value is over four times higher than that of the OFETs based on RT-DPh films with a dominant face-on orientation. **Figure S**2 correspondingly illustrates the typical output curves of the DPh-DNTT devices under different temperatures. No obvious distortions were observed at the beginning of these curves, indicating the good contact between the gold electrodes and organic semiconductors. On the other hand, the intrinsic out-of-plane hole mobility ($\mu_{\perp}$) estimated by the space charge limited current (SCLC) method showed an opposite trend compared to the $\mu_{/\!/}$ (**Figure S**3 and 4). The $\mu_{\perp}$ increased with the decrease of temperature and the RT-DPh film showed a highest $\mu_{\perp}$ of 3.3 $\times 10^{-2}$ $cm^2V^{-1}s^{-1}$, which is in accordance with the evolutionary trend of molecular orientation at different deposition temperatures. In the case of RT-DPh, the vertical charge transport is significantly enhanced by benefiting from the face-on orientation with the π–π stacking direction towards the out-of-plane direction.

To advance the insights into the orientation transformation of DPh-DNTT films, we further performed transmission electron microscopy (TEM) and select area electron diffraction (SAED) analyses and the results of the DPh-DNTT thin films prepared under different deposition conditions are given in **Figure 3**a-d. We noticed that the topography of these films were apparently different with varied proportions of light and dark gray areas. The color contrast in the bright-field TEM images mainly stem from the diffraction contrast of different crystal orientation.[36] Therefore, local mapping of the molecular orientation in these films was performed by using high-resolution TEM

(HRTEM). As shown in **Figure 3**e-h, clear lattice fringes were observed in the dark gray region; in contrast, no obvious crystal lattice fringes were found in the light gray region. The measured distance between these fringes (~2.35 nm) suggests the diffraction fringes were originated from the (001) planes, which is equal to the length of DPh-DNTT molecules along the crystallographic c-axis. The diffraction fringe from (001) planes occurs only when (001) planes are nearly parallel to the incident electron beam, indicating that the molecules are lying down and exhibit a face-on arrangement. Furthermore, by reducing the substrate temperature, the ratio of face-on orientation was significantly increased, from none in HT-DPh films to around 60% in RT-DPh films (**Figure S**5). This is in good agreement with the GIWAXS observation that intensive (*00l*) peaks were detected in the in-plane direction when films are obtained at room temperature. The corresponding SAED patterns are also displayed in **Figure 3**i-l. The clear (001) diffraction ring in **Figure 3**l further demonstrates the appearance of the achieved face-on orientation in RT-DPh films. **Figure 3**m-p schematically illustrates the evolution of the molecular orientations of DPh-DNTT thin films with variant ratios of face-on orientations under different temperatures. In short, the molecular orientation of DPh-DNTT films is dependent on the formation temperature. This temperature-dependent molecular alignment has been observed in other organic semiconductors such as DNTT as well.[37-39] By reducing the formation temperature to below 30 °C, a preferred face-on orientation of DPh-DNN films can thus be ensured, which results in a huge improvement in the out-of-plane hole mobility. The improvement of hole

mobility is likely to improve the potential of DPh-DNTT as a dopant-free HTM to obtain high photovoltaic performance.

In addition to an efficient hole mobility, a suitable highest occupied molecular orbital (HOMO) energy level is another important assessment criterion of the efficient HTMs used in PSCs. Previous studies have revealed that the ionization energy of organic compounds depends on the orientation of molecules.[40] Therefore, we investigated the HOMO level of HT-DPh and RT-DPh films by utilizing ultraviolet photoelectron spectroscopy (UPS). The detailed onset (E_{onset}) and cut-off (E_{cutoff}) energy edges of HT-DPh and RT-DPh films are given in **Figure 4**a and b, respectively. Based on the equation: $\Phi = 21.22 - (E_{cutoff} - E_{onset})$, the HOMO levels of HT-DPh and RT-DPh films were calculated to be -5.03 eV and -5.42 eV. The detailed evolution of HOMO levels under different substrate temperatures are shown in **Figure S**6. Obviously, the HOMO level shows a strong dependence on the molecular orientation of DPh-DNTT films. As the ratio of face-on orientation increases, the HOMO value of the film becomes smaller. The orientation-dependent HOMO levels were further rationalized by conducting the plane-wave based density-functional theory (DFT) calculations for single and multiple layers of standing-up or lying-down DPh-DNTT molecules. As shown in **Figure S**7, the bandgap center (BGC) of the standing-up DPh-DNTT layer is closer to the vacuum level position (E_v) compared with the lying one, i.e., the HOMO level of lying DPh-DNTT molecules is deeper than that of standing-up molecules, which is in good agreement with the UPS results. Moreover, the HOMO level position is nearly independent to the thickness of the thin film and it is found that

the molecular orientation allowed tuning the ionization energy of one molecule at most by 0.6 eV, which agrees well with the previous report.[40] In our wok, the experimental HOMO difference between RH-DPh and HT-DPh is 0.39 eV, which might be reasonable because of the residual standing molecules in RT-DPh films. The computational values of HOMO/LUMO for lying-down and standing-up DPh-DNTT layers are -5.50/-2.50 and -4.92/-1.92 eV, respectively, which are consistent with the measured results from UPS. The **Figure 4c** of electron density distribution in real space for HOMO and LUMO levels reveals that the electrons in both HOMO and LUMO levels are restricted to the center parts of DPh-DNTT molecules.

Referring to the valence band of $MAPbI_3$ perovskite (5.47 eV), RT-DPh exhibits a better-matched HOMO level, making it more suitable as HTMs for PSCs. As observed from the UV-Vis absorption spectra (**Figure S**8), the absorption peak of DPh-DNTT films at 487 nm, corresponding to the π-π^* intermolecular interaction, shows a 36 nm red-shift over the parent DNTT film due to the additional π-conjugated phenyl substitution at both terminals of the DNTT core. The extension of the π-conjugated systems allows the thermal stability of DPh-DNTT-based devices to be superior to that of DNTT- and C_{10}-DNTT-based devices. By subtracting the optical bandgap (E_g) estimated from the Tauc plot, the LUMO level of DPh-DNTT film is determined to be around -2.94 eV, which is shallow enough to block electron carriers. We also find that the optical bandgap is almost independent to the substrate temperature and the bandgap difference between RT-DPh and HT-DPh is less than 0.01eV (**Figure S**9). The energy level diagram is expressed in **Figure 4**d, in which RT-DPh exhibits a lower HOMO

position than that of HT-DPh. The smooth band alignment between the RT-DPh and perovskite layer enables an efficient and fluent hole extraction process during the work of PSCs. Moreover, the deeper HOMO level would enhance the open circuit voltage (V_{oc}) of PSC devices.[41]

The thermal properties of DPh-DNTT were also studied by conducting differential scanning calorimetry (DSC) and thermogravimetric (TG) measurements simultaneously. A small glass transition temperature (T_g) step was observed at 185 °C (**Figure 4**e), which is much higher than that of pristine spiro-OMeTAD (121 °C).[7] Meanwhile, the endothermic peak at 448 °C indicates a higher melting point of DPh-DNTT compared with spiro-OMeTAD (246 °C); the DPh-DNTT kept stable up to the sublimation temperature of 500 °C. This good thermal stability can also be seen from the TG curve, which exhibits a higher decomposition temperature (with 5% mass loss, T_d) of 497 °C as compared to spiro-OMeTAD (437 °C).[7] In addition, the surface wettability of DPh-DNTT was investigated by contact angle measurement using different solutions. As shown in **Figure S10**, the measured water contact angle (~105°) is as large as the common organic HTMs such as PTAA,[42] which can benefit the long-term stability by precluding water permeation. The measured contact angles of DMF and $MAPbI_3$ are much lower (~20°), showing relatively hydrophilic surface property compared with P_3HT.[42] This moderate wettability to the perovskite solution potentially facilitates the formation of high-quality perovskite film and tight interface between DPh-DNTT and perovskite layer.

The inverted PSCs with a planar configuration of ITO/DPh-DNTT/perovskite/$PC_{61}BM$/bathocuproine (BCP)/Ag (**Figure 5**a) were fabricated to examine the capacity of pristine DPh-DNTT films as effective HTMs. Considering the enough databases for comparison, we chose a commonly used $MAPbI_3$ as perovskite absorber that was prepared by one-step antisolvent method.[43-44] Firstly, we investigated the effect of DPh-DNTT thickness on the photovoltaic performance of PSCs. As shown in **Figure S**11, PSCs based on a 30 nm thick of DPh-DNTT layer showed the best performance, which might be due to the balance of the transmittance and series resistance. **Figure 5**b shows a cross-sectional SEM image of the RT-DPh-based device. A layer of RT-DPh with a thickness of around 30 nm is uniformly deposited between the substrate and perovskite film. Based on the optimized thickness, the current-voltage (*J-V*) characteristics of the champion cells with DPh-DNTT films deposited at different substrate temperatures are given in **Figure 5**c. Moreover, the statistic study of temperature-dependent performances of DPh-DNTT-based devices were summarized in **Figure S**12. It can be noticed that the short-circuit current density (J_{sc}) and V_{oc} increased with decreasing the deposition temperature. The enlarged V_{oc} (from 0.95 V to 1.09V) is ascribed to the decreased HOMO levels caused by the face-on orientation. The deeper HOMO level HTMs exhibited higher recombination resistance and thus much lower charge recombination rate, resulting in higher V_{oc} values.[41] The change of J_{sc} can be explained from aspects of hole mobility, perovskite crystallinity and interface quality. As the hole mobility $\mu_{\perp}$ of the RT-DPh film is over five times higher than that of HT-DPh film, which facilitates a more efficient charge

separation and transportation and thus enables a higher photocurrent density for RT-DPh-based PSCs. Furthermore, the perovskite morphology and crystal quality were examined by SEM and XRD. As shown in **Figure 5**d and e, the perovskite crystal coated on RT-DPh films had a larger grain size than on HT-DPh films; the higher intensity of perovskite (110) and (220) peaks on RT-DPh films also indicated a better perovskite crystallinity (**Figure 5**f), which could be due to the fact that lying-down DPh-DNTT molecules lead to the reduced grain boundaries and better interfacial interaction. It is worth mentioning that a unique and evident peak at around 18.3° appeared in the XRD profile of RT-DPh, which corresponds to the (110) plane of DPh-DNTT crystals. This extra peak suggested the existence of lying down molecules with a π-π interaction along the surface normal, correlating well with the former results of GIWAXS. Here, the RT-DPh based PSCs showed a champion PCE of 20.18% with negligible hysteresis and an excellent V_{oc} of 1.104 V; the detailed parameters of the champion cell are given in **Figure 5**g. Meanwhile, a stabilized PCE of 19.92% with a smooth current density of 21.42 mA/cm^2 was recorded near the maximum power point with an applied voltage bias of 0.93 V after 10-minute duration for the champion device as shown in **Figure 5**h, which further confirmed the reliability of the obtained champion-efficiency from the *J-V* characteristic. Furthermore, the corresponding external quantum efficiency (EQE) spectrum of the champion device is shown in **Figure 5**i in which the integrated photocurrent density matches well with the J_{sc} obtained from *J-V* measurement with a less than 5% mismatch. To the best of our knowledge, this high PCE is among the highest reported efficiencies of $MAPbI_3$ PSCs

based on non-doped organic HTMs. **Figure 6**a summarized the PCE evolution of $MAPbI_3$-based PSCs according to the reported works using various dopant-free molecular HTMs; details are given in **Table S**1. One can easily notice that very few reported organic HTMs can achieve a high efficiency around 20% as well as a large V_{oc} value over 1.10 V based on $MAPbI_3$ perovskite absorber.

To gain an in-depth understanding of the hole extraction by RT-DPh, both steady-state photoluminescence (PL) and time-resolved PL (TRPL) measurements were conducted to examine the charge transfer process at the perovskite/HTM interface. As shown in **Figure 6**b, the PL spectra of $MAPbI_3$ film deposited on the bare ITO surface exhibits a typical emission peak at ~ 767 nm. By inserting a DPh-DNTT layer as the HTM, it can significantly quench the photoluminescence of perovskite by 90% owing to the effective hole extraction from the perovskite layer. After normalizing the PL intensity (**Figure S**13), a slightly more blue-shifted peak was recognized in RT-DPh film (~762 nm) as compared to HT-DPh (~765 nm), suggesting that RT-DPh effectively passivated the trap states at the HTM/perovskite interface.[45] Moreover, such a more efficient hole extraction process was further validated by comparing their TRPL spectra, as shown in **Figure 6**c. All the obtained TRPL curves were well fitted by the bi-exponential equation $I(t) = A_1 \exp(-t/\tau_1) + A_2 \exp(-t/\tau_2)$, in which the fast decay (τ_1) attributes to the carrier extraction across the HTM/perovskite interface and the slow decay (τ_2) mainly corresponds to interface recombination losses.[18] The detailed fitting parameters were summarized in **Table S**2. As expected, the perovskite-only film showed a significant PL decay time (τ_{avg}) of 617.5 ns. After introducing DPh-DNTT

HTM, the value of τ_{avg} is notably reduced to 277.5 ns (HT-DPh) and 124.8 ns (RT-DPh). The short average decay lifetime of RT-DPh/perovskite bilayer proved the effective charge extraction capability of RT-DPh film. Meanwhile, the interface recombination losses are greatly suppressed at the RT-DPh/perovskite interface compared with the HT-DPh/perovskite interface. In exploration of the performance differences between RT-DPh- and HT-DPh-based PSCs, the DFT method was employed to investigate the charge transfer processes by calculating the charge distribution at HTM/perovskite interface. Here, the charge transfer difference is studied based on the lying down and standing up DPh-DNTT molecules, as shown in **Figure 6**d and e. For both cases, charge transfer is limited to the contact area between DPh-DNTT molecules and the perovskite surface. The lying-down molecule can be in full contact with the perovskite surface and the standing-up DPh-DNTT molecule is in contact with the perovskite surface by only its end part. Considering that both HOMO and LUMO levels of DPh-DNTT molecule are restricted to the center part (**Figure 4**c), it is expected that the hole extraction from the perovskite layer can be promoted by the lying-down case.

Since sulfur (S) atoms are believed to easily interact with lead (Pb) atoms, people have developed many S-containing moieties or molecules to passivate defects of the perovskite through forming salutary S-Pb interactions.[46-48] In our case, the two S-bearing thiophene rings of DPh-DNTT molecules could passivate the defects at the perovskite/HTM interface. The X-ray photoelectron spectroscopy (XPS) and Fourier transform infrared (FTIR) spectroscopy were used to verify the interaction between the S-contained DPh-DNTT molecules and lead-based perovskites. As shown in **Figure 6**f,

both Pb $4f_{7/2}$ and $4f_{5/2}$ peaks of the perovskite/DPh-DNTT bilayer display an apparent shift of 0.25 eV towards lower binding energy compared to the pristine perovskite (Pb $4f_{7/2}$, 138.47 and Pb $4f_{5/2}$, 143.40 eV).[46] This distinct red shift is caused by the increased electron density around Pb^{2+}, which indicates the formation of S-Pb coordination through electron cloud overlap. A blue shift is also observed in the S 2p spectrum (**Figure 6**g) in which the S $2p_{3/2}$ peak shifted from 164.04 to 164.24 eV and S $2p_{1/2}$ peak shifted from 165.22 eV to 165.42 eV, evidencing the existence of strong S-Pb interaction.[46]

To probe the S-Pb interaction at the DPh-DNTT /perovskite interface, the FTIR spectrum of pure DPh-DNTT, PbI_2 and the mixed film of DPh-DNTT/PbI_2 were analyzed. As shown in **Figure S**14, characteristic bands of the thiophene moiety in the DPh-DNTT structure are located at around 700 cm^{-1} and 600 cm^{-1}, which attribute to the C-H out-of-plane vibration and C-S-C stretching, respectively.[49] After blending with PbI_2 material, two additional absorption peak at 462 cm^{-1} and 454 cm^{-1} are observed, indicating the existence of interaction of DPh-DNTT molecules and Pb^{2+} in the perovskite structure. Overall, these XPS and FTIR results clearly demonstrated the formation of S-Pb coordination bond at the interface between DPh-DNTT and perovskite, which can enhance the hole extraction efficiency as well as passivate trap states like Pb defects at the interface.[48] Additionally, the S-Pb interaction can also modulate the crystal growth of upper perovskite layer with large grains and high crystallinity according to our observations in SEM images and XRD patterns.[48] The

strong interfacial interaction would also benefit the stabilization of the perovskite layer and thus the long-term stability.

Figure S15 shows the device stability of RT-DPh-based PSCs, where the unencapsulated device can still hold over 90% of its initial efficiency after aging at room temperature with a relative humidity of 60% ± 10% for 45 days. As seen, the DPh-DNTT-based perovskite film was stable in air for 45 days without obvious color change due to the strong S-Pb coordination at HTM/perovskite interface as well as the hydrophobicity of DPh-DNTT. In contrast, a severe collapse of the perovskite occurred in the referred perovskite/ITO sample, showing a large area of brown region and an extra-strong PbI_2 peak in the XRD profile within 5 days. Toward commercialization, the thermal stability of PSC is critical to the rigorous working temperature in outdoor conditions.[50] The typical device based on the common HTMs, Spiro-OMeTAD, P_3HT and PTAA, showing a rapid degradation at a temperature of 80 °C.[51] The instability is mainly caused by the selective HTMs while the $MAPbI_3$ perovskite itself has proved to be thermally stable.[50] Therefore, the thermal stability of perovskite film with DPh-DNTT was examined by heating at 85 ℃ in the air, where the film was encapsulated with epoxy in the nitrogen glove box. The absorbance spectra of **Figure S**16 shows that no obvious change was observed after heat-treatment for 15 days, indicating that the excellent thermotolerance of DPh-DNTT led to the superior thermal-stability of the film.[32]

In summary, we report the temperature-dependent molecular orientation of organic DPh-DNTT semiconductor as an effective dopant-free HTM for high-efficiency PSCs. The face-on molecular orientation can be engineered by controlling the substrate temperature during the vacuum evaporation process, of which RT-DPh reached an out-of-plane mobility of 3.3×10^{-2} $cm^2V^{-1}s^{-1}$, surpassing the HTMs reported so far. The PSCs equipped with pristine RT-DPh HTM achieved an excellent PCE of of 20.2% with improved parameters (J_{sc}, V_{oc} and *FF*) due to the deeper HOMO level, higher out-of-plane hole mobility, better interface interaction and more efficient charge transfer, which is at the forefront performance compared with the reported $MAPbI_3$-based PSCs. Benefiting from the excellent hydrophobicity of DPh-DNTT and the formation of S-Pb coordination at the DPh-DNTT/perovskite interface, the RT-DPh-based cells performed a superior long-term stability. Our work provides insights into temperature-dependent π-π stacking orientation and opens a route to apply the organic semiconductors as promising HTL or ETL materials for PSCs.

Experimental Section

Experimental details are provided in the Supporting Information.

Supporting Information

Supporting Information is available from the Wiley Online Library or from the author.

Acknowledgements

This work was supported by the General Research Fund of the Research Grants Council of Hong Kong Special Administrative Region, China under award number 17206519. This work was also supported by the Seed Fund for Strategic Interdisciplinary Research

Scheme at the University of Hong Kong and HKU-Zhejiang Institute of Research and Innovation (HKU-ZIRI). The authors also thank Dr. Wenshu Yang from the Harbin Institute of Technology for his support and assistance on the DSC and TG measurements. For the TEM and HRTEM experiments, the authors acknowledge Mr. Frankie Y. F. Chan from the Electron Microscopy Unit of HKU for his professional handling skills of TEM equipment. The authors would also like to thank Mr. Wing Kin Ho from the Department of Physics of HKU for his kind and patient assistance on UPS and XPS tests. H.Z. is grateful for financial support from the European Union's Horizon 2020 research and innovation programme under grant agreements No 881603 (Graphene Flagship Core 3).

Conflict of Interest

The authors declare no conflict of interest.

Received: ((will be filled in by the editorial staff))
Revised: ((will be filled in by the editorial staff))
Published online: ((will be filled in by the editorial staff))

Reference

[1] A. Kojima, K. Teshima, Y. Shirai, T. Miyasaka, *J. Am. Chem. Soc.* **2009**, 131, 6050.
[2] S. D. Stranks, G. E. Eperon, G. Grancini, C. Menelaou, M. J. Alcocer, T. Leijtens, L. M. Herz, A. Petrozza, H. J. Snaith, *Science* **2013**, 342, 341.
[3] W. Tress, N. Marinova, O. Inganäs, M. K. Nazeeruddin, S. M. Zakeeruddin, M. Graetzel, *Adv. Energy Mater.* **2015**, 5, 1400812.
[4] W. S. Yang, J. H. Noh, N. J. Jeon, Y. C. Kim, S. Ryu, J. Seo, S. I. Seok, *Science* **2015**, 348, 1234.
[5] D. Bi, W. Tress, M. I. Dar, P. Gao, J. Luo, C. Renevier, K. Schenk, A. Abate, F. Giordano, J.-P. C. Baena, *Sci. Adv.* **2016**, 2, e1501170.
[6] M. Saliba, T. Matsui, J.-Y. Seo, K. Domanski, J.-P. Correa-Baena, M. K. Nazeeruddin, S. M. Zakeeruddin, W. Tress, A. Abate, A. Hagfeldt, *Energy Environ. Sci.* **2016**, 9, 1989.
[7] N. J. Jeon, H. Na, E. H. Jung, T.-Y. Yang, Y. G. Lee, G. Kim, H.-W. Shin, S. I. Seok, J. Lee, J. Seo, *Nat. Energy* **2018**, 3, 682.

[8] Q. Jiang, Y. Zhao, X. Zhang, X. Yang, Y. Chen, Z. Chu, Q. Ye, X. Li, Z. Yin, J. You, *Nat. Photonics* **2019**, 1.
[9] N. Ahn, D.-Y. Son, I.-H. Jang, S. M. Kang, M. Choi, N.-G. Park, *J. Am. Chem. Soc.* **2015**, 137, 8696.
[10] D.-Y. Son, S.-G. Kim, J.-Y. Seo, S.-H. Lee, H. Shin, D. Lee, N.-G. Park, *J. Am. Chem. Soc.* **2018**, 140, 1358.
[11] N. J. Jeon, J. H. Noh, W. S. Yang, Y. C. Kim, S. Ryu, J. Seo, S. I. Seok, *Nature* **2015**, 517, 476.
[12] J.-P. Correa-Baena, A. Abate, M. Saliba, W. Tress, T. J. Jacobsson, M. Grätzel, A. Hagfeldt, *Energy Environ. Sci.* **2017**, 10, 710.
[13] W. Zhou, Z. Wen, P. Gao, *Adv. Energy Mater.* **2018**, 8, 1702512.
[14] W. S. Yang, B.-W. Park, E. H. Jung, N. J. Jeon, Y. C. Kim, D. U. Lee, S. S. Shin, J. Seo, E. K. Kim, J. H. Noh, *Science* **2017**, 356, 1376.
[15] M. Saliba, S. Orlandi, T. Matsui, S. Aghazada, M. Cavazzini, J.-P. Correa-Baena, P. Gao, R. Scopelliti, E. Mosconi, K.-H. Dahmen, *Nat. Energy* **2016**, 1, 15017.
[16] T. H. Schloemer, J. A. Christians, J. M. Luther, A. Sellinger, *Chem. Sci.* **2019**, 10, 1904.
[17] Z. Yu, L. Sun, *Small Methods* **2018**, 2, 1700280.
[18] Y. Wang, W. Chen, L. Wang, B. Tu, T. Chen, B. Liu, K. Yang, C. W. Koh, X. Zhang, H. Sun, *Adv. Mater.* **2019**, 31, 1902781.
[19] E. Rezaee, X. Liu, Q. Hu, L. Dong, Q. Chen, J. H. Pan, Z. X. Xu, *Solar RRL* **2018**, 2, 1800200.
[20] X. Yin, J. Zhou, Z. Song, Z. Dong, Q. Bao, N. Shrestha, S. S. Bista, R. J. Ellingson, Y. Yan, W. Tang, *Adv. Funct. Mater.* **2019**, 29, 1904300.
[21] K. Rakstys, C. Igci, M. K. Nazeeruddin, *Chem. Sci.* **2019**, 10, 6748.
[22] E. H. Jung, N. J. Jeon, E. Y. Park, C. S. Moon, T. J. Shin, T.-Y. Yang, J. H. Noh, J. Seo, *Nature* **2019**, 567, 511.
[23] C. Wang, H. Dong, L. Jiang, W. Hu, *Chem. Soc. Rev.* **2018**, 47, 422.
[24] K. Takimiya, I. Osaka, T. Mori, M. Nakano, *Acc. Chem. Res.* **2014**, 47, 1493.
[25] K. Gao, B. Xu, C. Hong, X. Shi, H. Liu, X. Li, L. Xie, A. K. Y. Jen, *Adv. Energy Mater.* **2018**, 8, 1800809.
[26] K. Rakstys, S. Paek, P. Gao, P. Gratia, T. Marszalek, G. Grancini, K. T. Cho, K. Genevicius, V. Jankauskas, W. Pisula, *J. Mater. Chem. A* **2017**, 5, 7811.
[27] L. Yang, F. Cai, Y. Yan, J. Li, D. Liu, A. J. Pearson, T. Wang, *Adv.Funct. Mater.* **2017**, 27, 1702613.
[28] S. Kazim, F. J. Ramos, P. Gao, M. K. Nazeeruddin, M. Grätzel, S. Ahmad, *Energy Environ. Sci.* **2015**, 8, 1816.
[29] J. Mai, Y. Xiao, G. Zhou, J. Wang, J. Zhu, N. Zhao, X. Zhan, X. Lu, *Adv.Mater.* **2018**, 30, 1802888.
[30] Z. Zhou, Q. Wu, S. Wang, Y. T. Huang, H. Guo, S. P. Feng, P. K. L. Chan, *Adv. Sci.* **2019**, 1900775.
[31] K. Niimi, M. J. Kang, E. Miyazaki, I. Osaka, K. Takimiya, *Org. Lett.* **2011**, 13, 3430.

[32] M. J. Kang, E. Miyazaki, I. Osaka, K. Takimiya, A. Nakao, *ACS Appl. Mater. Interfaces* **2013**, 5, 2331.
[33] A. K. Jena, A. Kulkarni, T. Miyasaka, *Chem. Rev.* **2019**, 119, 3036.
[34] T. Yokota, K. Kuribara, T. Tokuhara, U. Zschieschang, H. Klauk, K. Takimiya, Y. Sadamitsu, M. Hamada, T. Sekitani, T. Someya, *Adv. Mater.* **2013**, 25, 3639.
[35] J. W. Borchert, B. Peng, F. Letzkus, J. N. Burghartz, P. K. Chan, K. Zojer, S. Ludwigs, H. Klauk, *Nat. Commun.* **2019**, 10, 1119.
[36] J. Gilchrist, S. Heutz, D. McComb, *J. Phys. Conf. Ser.* **2012**, 371, 012042.
[37] F. Liscio, C. Albonetti, K. Broch, A. Shehu, S. D. Quiroga, L. Ferlauto, C. Frank, S. Kowarik, R. Nervo, A. Gerlach, *ACS Nano* **2013**, 7, 1257.
[38] M.-C. Jung, M. R. Leyden, G. O. Nikiforov, M. V. Lee, H.-K. Lee, T. J. Shin, K. Takimiya, Y. Qi, *ACS Appl. Mater. Interfaces* **2015**, 7, 1833.
[39] K. Pei, X. Ren, Z. Zhou, Z. Zhang, X. Ji, P. K. L. Chan, *Adv. Mater.* **2018**, 30, 1706647.
[40] S. Duhm, G. Heimel, I. Salzmann, H. Glowatzki, R. L. Johnson, A. Vollmer, J. P. Rabe, N. Koch, *Nat. Mater.* **2008**, 7, 326.
[41] W. Yan, Y. Li, S. Ye, Y. Li, H. Rao, Z. Liu, S. Wang, Z. Bian, C. Huang, *Nano Res.* **2016**, 9, 1600.
[42] Q. Lin, D. M. Stoltzfus, A. Armin, P. L. Burn, P. Meredith, *Adv. Mater. Interfaces* **2016**, 3, 1500420.
[43] W. E. Sha, H. Zhang, Z. S. Wang, H. L. Zhu, X. Ren, F. Lin, A. K. Y. Jen, W. C. Choy, *Adv.Energy Mater.* **2018**, 8, 1701586.
[44] R. Cheng, C. C. Chung, H. Zhang, F. Liu, W. T. Wang, Z. Zhou, S. Wang, A. B. Djurišić, S. P. Feng, *Adv. Energy Mater.* **2019**, 1901980.
[45] Y. Shao, Z. Xiao, C. Bi, Y. Yuan, J. Huang, *Nat. Commun.* **2014**, 5, 1.
[46] Y. Yan, S. Yu, A. Honarfar, T. Pullerits, K. Zheng, Z. Liang, *Adv. Sci.* **2019**, 6, 1900548.
[47] S. Yang, S. Chen, E. Mosconi, Y. Fang, X. Xiao, C. Wang, Y. Zhou, Z. Yu, J. Zhao, Y. Gao, *Science* **2019**, 365, 473.
[48] K. Jiang, J. Wang, F. Wu, Q. Xue, Q. Yao, J. Zhang, Y. Chen, G. Zhang, Z. Zhu, H. Yan, *Adv. Mater.* **2020**, 32, 1908011.
[49] C. Rassie, R. A. Olowu, T. T. Waryo, L. Wilson, A. Williams, P. G. Baker, E. I. Iwuoha, *Int. J. Electrochem. Sci.* **2011**, 6, 1949.
[50] X. Zhao, H.-S. Kim, J.-Y. Seo, N.-G. Park, *ACS Appl. Mater. Interfaces* **2017**, 9, 7148.
[51] S. N. Habisreutinger, T. Leijtens, G. E. Eperon, S. D. Stranks, R. J. Nicholas, H. J. Snaith, *Nano Lett.* **2014**, 14, 5561.

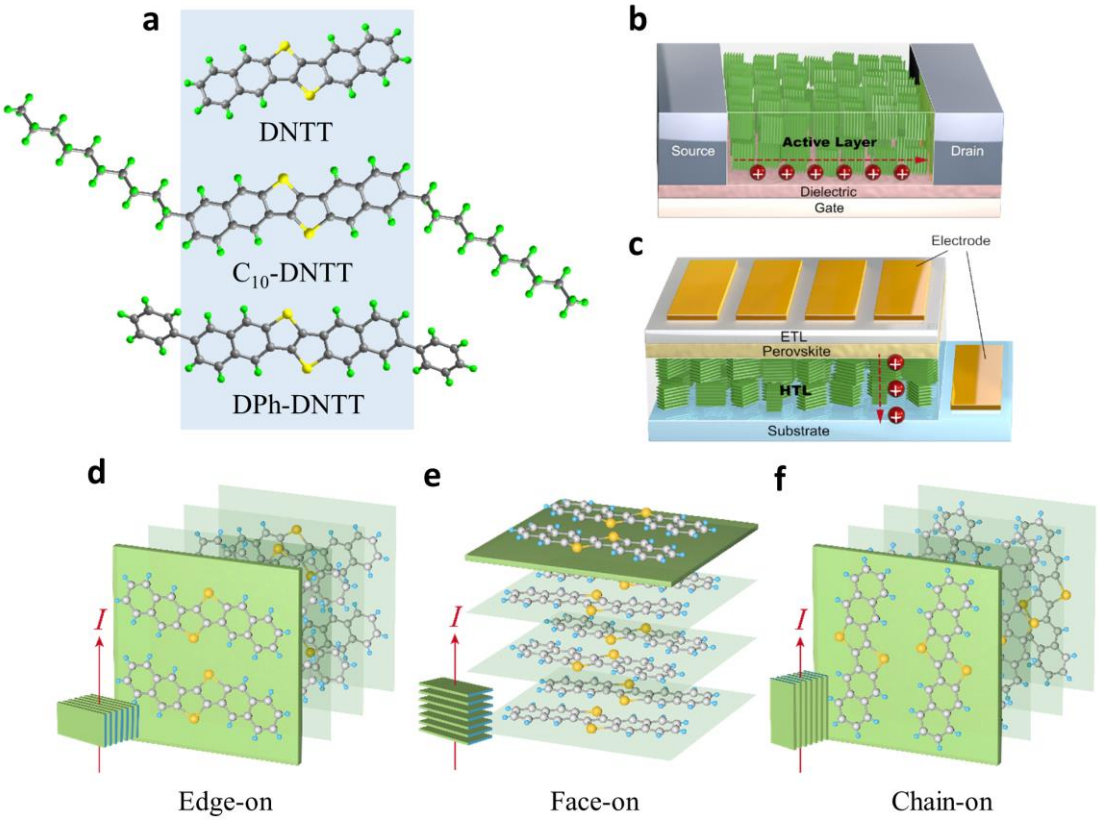

Figure 1. (a) Molecular structures of DNTT, C_{10}-DNTT and DPh-DNTT. (b) Schematic structure of an OFET device based on p-type semiconductors. (c) Schematic structure of a planar inverted PSC device with electron/hole-transporting layers (ETL/HTL). (d)-(f) Schematic diagrams of edge-on, face-on, and chain-on orientations of organic semiconductors.

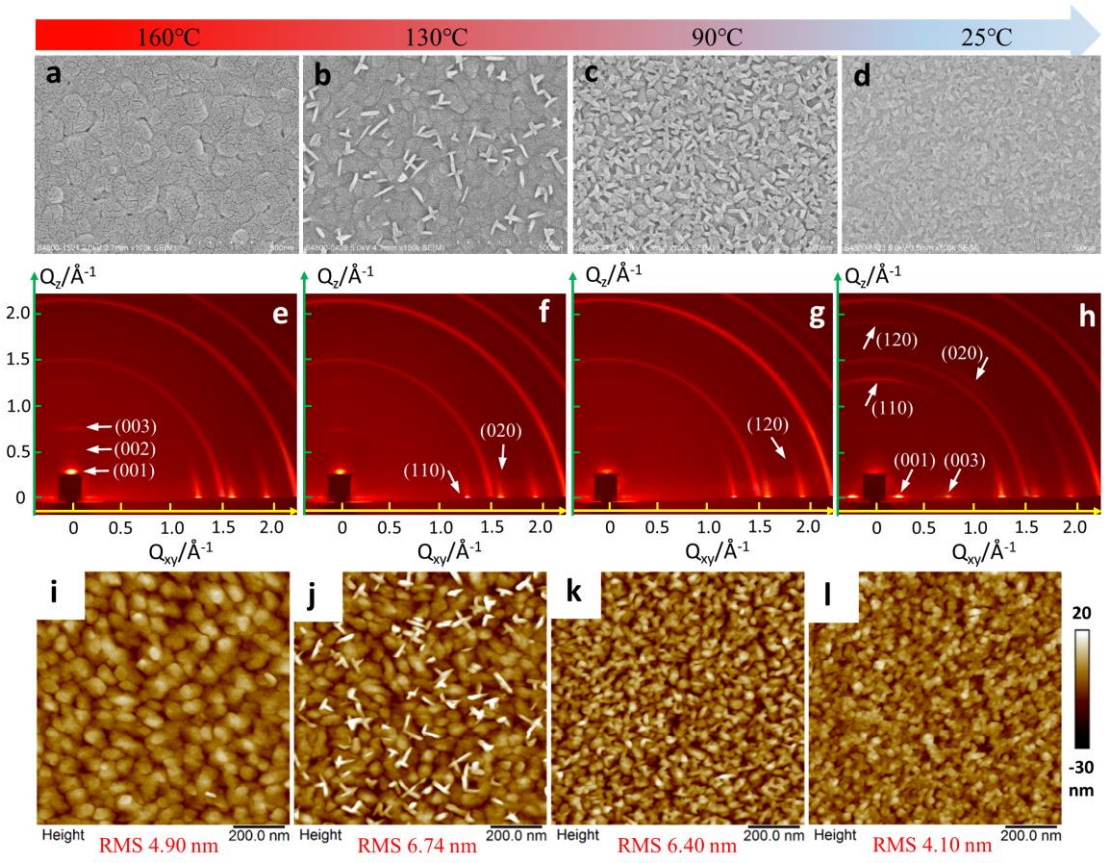

Figure 2. (a)-(d) SEM study of the surface morphology of DPh-DNTT thin films fabricated by thermal evaporation in vacuum under different ITO-substrate temperatures. (e)-(h) The corresponding GIWAXS patterns of these films. The grazing incident angle is fixed at 0.2° during the GIWAXS measurement. (i)-(l) The corresponding surface profiles of these films measured by AFM.

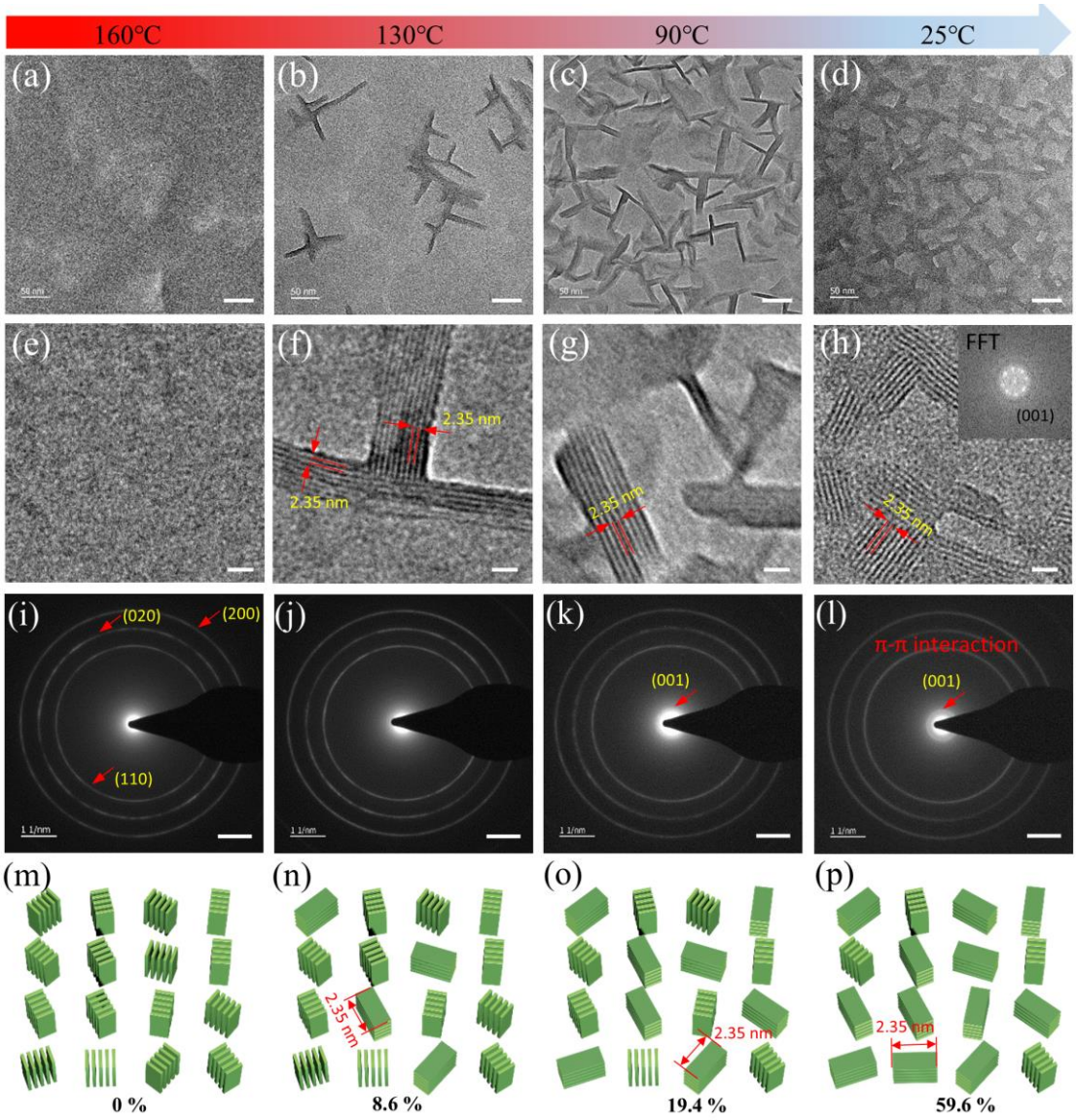

Figure 3. (a)-(d) Top-view TEM images of DPh-DNTT thin films prepared under different substrate temperatures. The TEM images are captured in bright field mode with a scale bar of 50 nm. (e)-(h) Corresponding high-resolution TEM (HRTEM) images of these films with a scale bar of 5 nm. The inset picture is the transformed diffraction pattern of (h) by using a fast Fourier transform (FFT). (i)-(l) Corresponding SAED patterns with a scale bar of 1 1/nm. (m)-(p) Corresponding schematics of crystal orientation with the combination of face-on and chain-on orientations in different proportions.

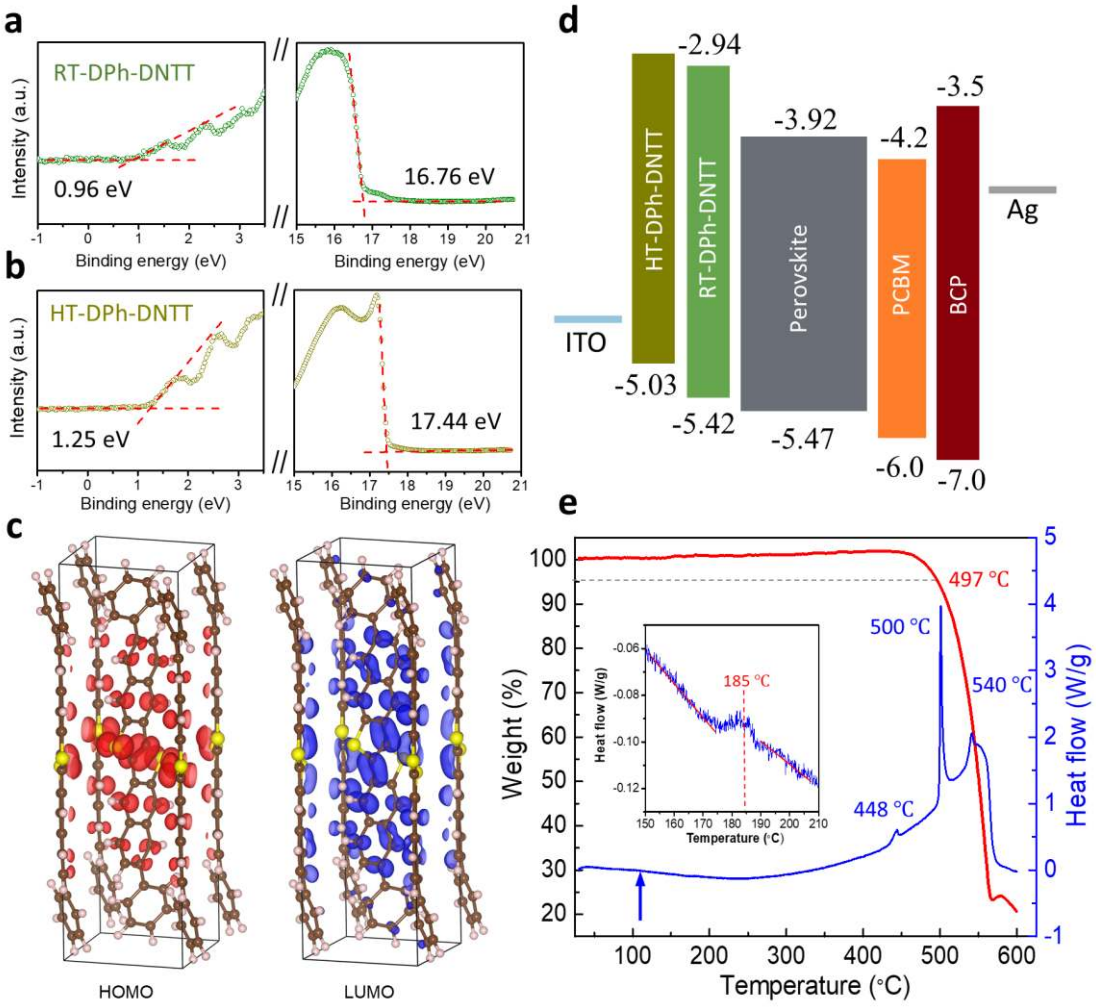

Figure 4. (a) UPS results of the RT-DPh thin film. The former curve is the onset energy region and the latter one shows the cutoff energy region. (b) UPS results of the referred HT-DPh thin film. (c) The electronic distribution of HOMO (in red) and LUMO (in blue) for the DPh-DNTT crystal. The primitive simulation cell is indicated by the solid black lines. The isosurface value of 0.002 e/Å^3 is used. The C, H and S atoms are represented by brown, pink and yellow spheres, respectively. (d) Energy level diagram of perovskite devices based on pristine RT-DPh and HT-DPh semiconductors. (e) TG (red curve) and DSC (blue curve) results of DPh-DNTT measured in nitrogen atmosphere at a scan rate of 5 °C/min. The vertical arrow indicates the endothermic reaction processes. The amplified inset profile shows the glass transition step with a high T_g of 185 °C.

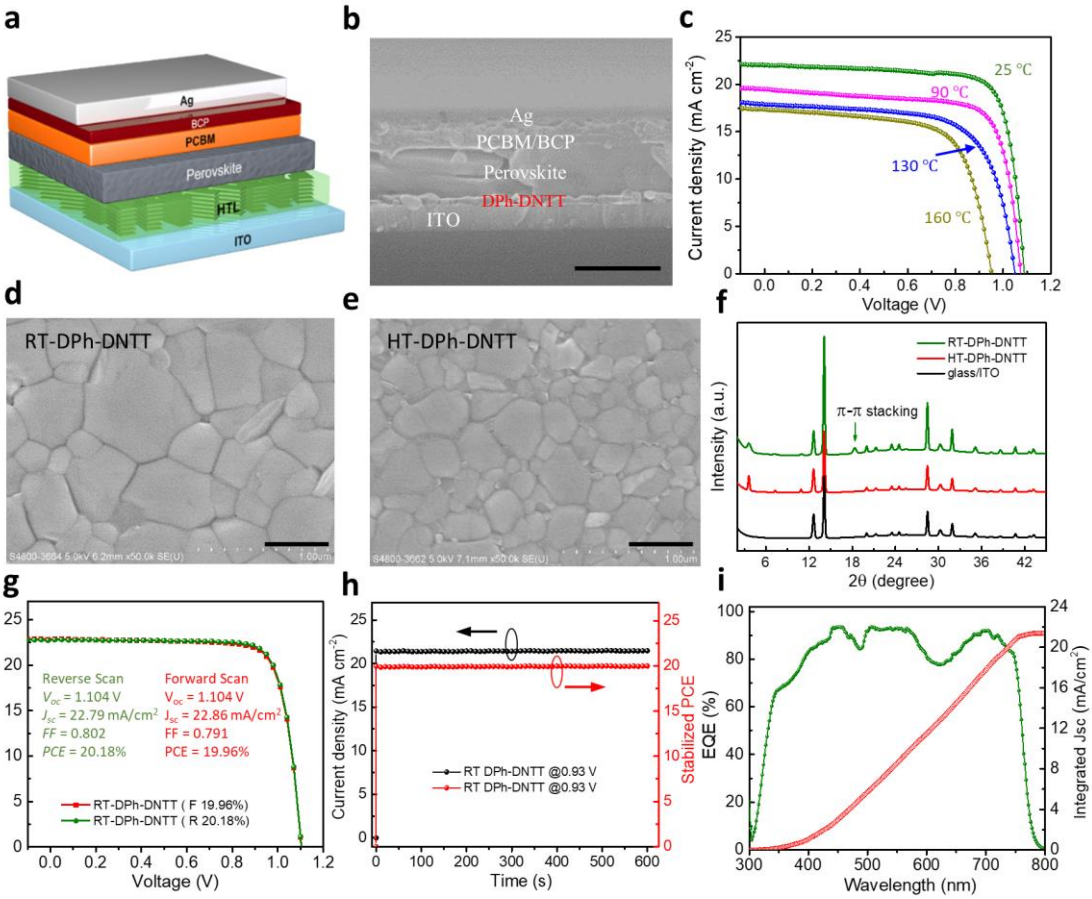

Figure 5. (a) The sketch of the inverted device structure. (b) SEM image of the cross-section. (c) The *J-V* curves of devices with dopant-free DPh-DNTT films prepared under different substrate temperatures. (d) Top-view SEM images of perovskite crystals on RT-DPh and (e) on HT-DPh layers. (f) The general XRD results of perovskite without/with DPh-DNTT films. (g) The *J-V* curves of the champion solar cell based on the RT-DPh as the HTM. (h) Stabilized PCE and photocurrent density near the maximum power point with an applied voltage bias of 0.93 V for 600 s. (i) EQE spectrum with the integrated short-circuit current density for the RT-DPh-based $MAPbI_3$ perovskite solar cell.

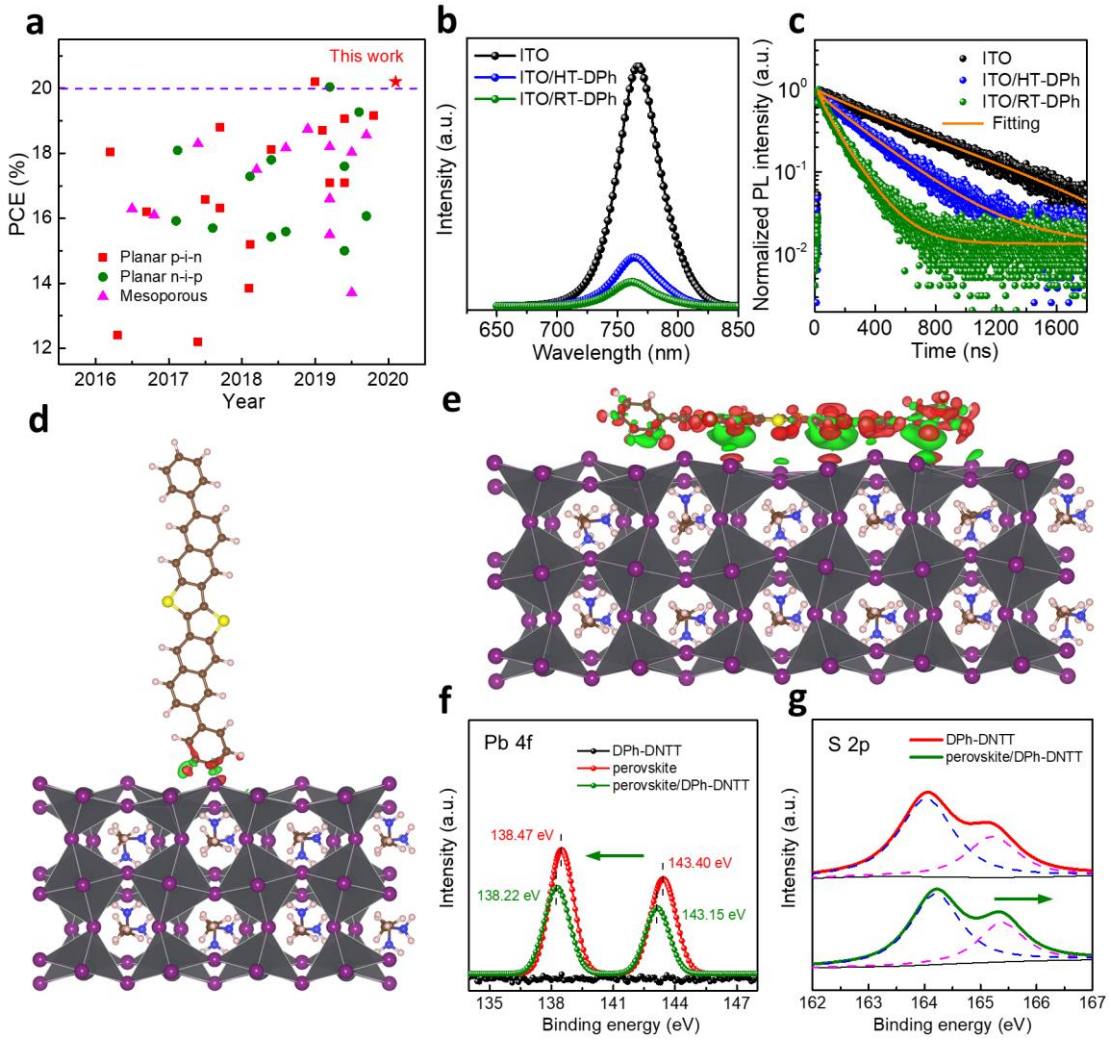

Figure 6. (a) Summarized PCE evolution of $MAPbI_3$-based solar cells employing various dopant-free small-molecule HTMs. Details are given in Table S1. (b) Steady-state photoluminescence (PL) profiles and (c) normalized time-resolved PL decay spectra of perovskite films coated on different substrates. Charge density differences for adsorption of DPh-DNTT molecule on the $MAPbI_3$ (110) surface with molecule standing up (d) and lying down(e), respectively. The C, H, N, Pb, I, S atoms are represented by brown, pink, blue, dark grey, purple and yellow spheres, respectively. The PbI_6 octahedron is indicated by filled grey color. Green area indicates electron accumulation, while rea area represents for electron depletion. The isosurface value of 0.0005 e/Å^3 is used. The obtained XPS spectra of (f) Pb 4*f* and (g) S 2*p* region of DPh-DNTT, perovskite and perovskite/DPh-DNTT bilayer.

Supporting Information

Tunable π-π Stacking of Organic Small Molecules as Dopant-Free Hole Transport Materials for High-Performance Perovskite Solar Cells

Zhiwen Zhou[1], Qisheng Wu[2], Rui Cheng[1], Hong Zhang[3], Sijia Wang[1], Mojun Chen[1], Maohai Xie[4], Paddy Kwok Leung Chan[1], Michael Grätzel[3*] and Shien-Ping Feng[1*]*

[1]Department of Mechanical Engineering, The University of Hong Kong, Pokfulam Road, Hong Kong, PR China.

[2] Department of Chemical Engineering and Materials Science, Michigan State University, East Lansing, Michigan 48824, United States.

[3] Laboratory of Photonics and Interfaces, Institute of Chemical Sciences and Engineering, École Polytechnique Fédérale de Lausanne Station 6, CH-1015 Lausanne, Switzerland

[4] Department of Physics, The University of Hong Kong, Pokfulam Road, Hong Kong, PR China.

Correspondence and requests for materials should be addressed to Prof. S. P. Feng (hpfeng@hku.hk) , Prof. Michael *Grätzel* (michael.graetzel@epfl.ch) or Prof. P. K. L. Chan (email: pklc@hku.hk)

Experimental methods

Materials

CH_3NH_3I (MAI) was purchased from Greatcell Solar Materials while lead iodine (PbI_2, high purity of 99.99%) and lead chloride ($PbCl_2$, high purity of 99.99%) were purchased from the TCI company. High purity of DPh-DNTT (99.9%) semiconductor powder was purchased from Luminescence Technology Corporation. Anhydrous dimethylformamide (DMF, 99.8%), 1,2-dichlorobenzene (DCB, 99%) and chlorobenzene (CB, 99.8%) solvents were purchased from Sigma-Aldrich. All the chemicals and solvents are used as received unless with further notes.

Device Fabrication

ITO substrates were sequentially cleaned by DI water with detergent, ethanol and isopropanol (IPA) for 5-10 minutes each. A thin film of DPh-DNTT was then deposited on the ITO by thermal evaporation at a low deposition rate of ~ 0.01 nm per second under a pressure of ~10^{-6} torr. To modulate the molecular orientation, the ITO substrate was heated to be various temperatures ranging from 25 ℃ to 160 ℃ during the evaporation process and the substrate was taken out from the vacuum chamber when the temperate was slowly cooled down to ambient temperature. For the $MAPbI_3$ perovskite solution, it was obtained by dissolving 500 mg PbI_2, 30 mg $PbCl_2$ and 190 mg MAI in 1ml DMF solvent and it was stirred at room temperature for 30 minutes within the nitrogen glove box. The obtained precursor solution was spun onto fresh DPh-DNTT covered-substrates at 4800 rpm for 15 s and 180 μL CB was rapidly dropped onto the substrate at the 5^{th} second. The fabricated perovskite wet film was then annealed at 100 ℃ for 10 minutes. After that, a thin layer of $PC_{61}BM$ was spin-coated on the top of perovskites at 1500 rpm for 60 s and 4000r for 5 s followed by an annealing treatment at 45 ℃ for 10 minutes. For the $PC_{61}BM$ solution, 20 mg $PC_{61}BM$

was dissolved into 1 ml DCB solvent. Before the final deposition of 100 nm Ag as electrodes in a vacuum chamber, 0.5 mg/ml BCP/ethanol solution was spin-coated onto the $PC_{61}BM$ film at 4000 rpm for 20 s. All the fabrication procedures were conducted at glove box unless otherwise stated.

Measurements and Characterizations

The surface morphology and grain size of the perovskite films were characterized by SEM technique. All SEM images were captured by a S4800 FEG (Hitachi) scanning electron microscope. For the TEM images and SAED patterns, they were captured by a Tecnai G2 20 S-TWIN transmission electron microscope with a high resolution of 2 Å. For the general XRD and 2D-GIWAXS measurements, they were performed using the *Rigaku SmartLab* 9 kW X-ray diffractometer (Cu target, $\lambda = 1.5406$ Å) with a highly sensitive *HyPix-3000* detector. Atomic force microscopy (AFM, Bruker, Multimode 8) was also used to characterize the surface morphology of the DPH-DNTT films. The thermal properties of DPh-DNTT semiconductor were analyzed by performing TGA-DSC measurements using a STA 449 F3 Jupiter (NETZSCH). The optical bandgap and HOMO level of DPh-DNTT films were measured by UV-vis spectroscopy (Lambda 35, Perkin Elmer) and XPS spectroscopy (Thermol Escalab 250 Xi, He I 21.22 eV radiation), respectively. DPh-DNTT-based OFETs were fabricated on the highly doped silicon wafer with 300 nm SiO_2 as the dielectric layer. The OFET devices were characterized by a Keithley 2636B sourcemeter with a programed LabView software. The field-effect mobility was calculated by the equation $I_{DS} = W/(2L) \cdot C_i \cdot \mu \cdot (V_G - V_T)^2$ in the saturation regime. On the other hand, the vertical mobility of DPh-DNTT films was extracted from the measured SCLC current with the help of a CHI660 electrochemical workstation. The vertical mobility was evaluated by the equation $J = (9/8) \cdot \varepsilon_0 \cdot \varepsilon_r \cdot \mu \cdot V^2_{eff}/d^3$, where J is the current density, ε_0 is the vacuum permittivity, ε_r is the relative permittivity, V_{eff} is the effective voltage and d is the film thickness. The

effective voltage can be obtained by subtracting the build-in voltage (V_{bi}) from the applied the voltage (V). The *J-V* curves of perovskite samples were recorded by PECL01 solar simulator using a standard AM 1.5G light illumination (100 mW/cm^2) calibrated with a certified Si reference cell and the illuminated device area is 0.1 cm^2. PL spectra and TRPL spectra were conducted with a FLS 980 spectrofluorometer (Edinburgh Instruments).

DFT calculation

The density functional theory (DFT) calculations were conducted with projector augmented wave (PAW)[1] pseudopotentials as embedded in the Vienna ab initio simulation (VASP) 5.4 package.[2] The optPBE-vdW functional[3] was used to properly describe the van der Waals interactions. The experimental bulk lattice parameters and atomic positions for T-phase[4] of $MAPbI_3$ were taken as input for DFT calculations. All systems were completely optimized until the energy and force were converged to be less than 10^{-5} eV and -0.05 eV/Å, respectively. The plane-wave cutoff energy was set to 400 eV for all calculations. For slab modeling, the vacuum space of > 15 Å was built to eliminate the interaction between periodic images. Electrostatic potential calculations were performed for DPh-DNTT slabs with few molecular layers, and two different contacting surfaces were simulated. For DPh-DNTT adsorption on the $MAPbI_3$ slab, the (110) surface with PbI termination was considered for the $MAPbI_3$ slab due to the fact that PbI is excessed in the device. The method proposed by Toroker et al.[5] to determine the band edge positions was employed in this work. The conduction band minimum (CBM) and valence band maximum (VBM) predicted by DFT calculations are given by: $E_{CBM/VBM} = E_{BGC} \pm 1/2\ E_g$, where E_{BGC} is the bandgap center energy for slabs calculated with the optPBE-vdW functional. E_g denotes the band gap of DPh-DNTT.

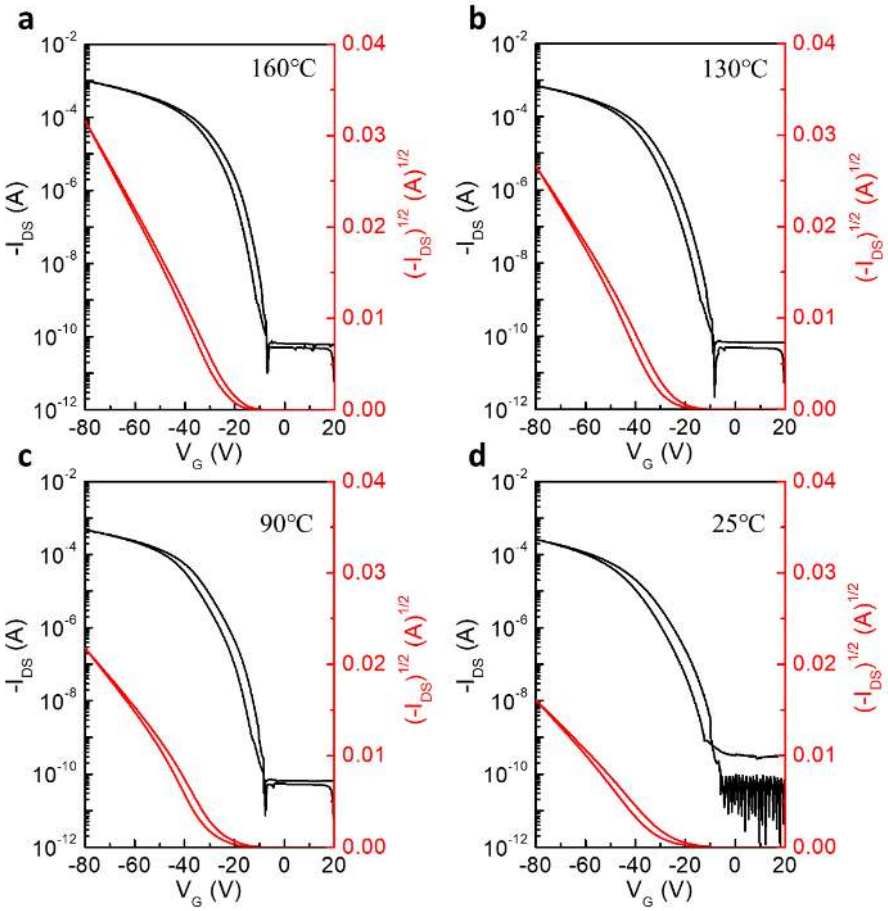

Figure S1. Transfer curves of OFETs based on evaporated DPh-DNTT films fabricated at different substrate temperatures. The channel length and width of the transistors are 76 (*L*) and 500 (*W*) μm, respectively. Prior to electrical measurements, all devices were isolated by mechanical scratches to avoid the overestimation of mobility caused by the fringe current. All the OFETs were characterized in a nitrogen glove box at room temperature.

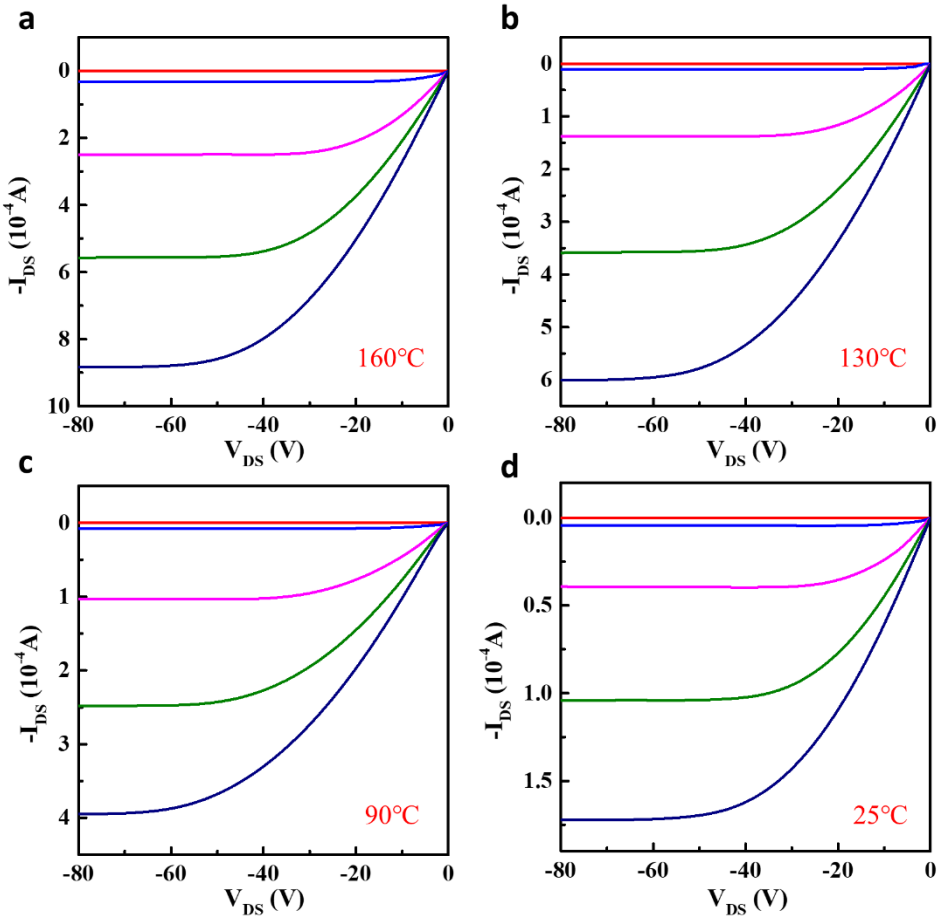

Figure S2. The corresponding output curves of OFETs based on evaporated DPh-DNTT films fabricated at different substrate temperatures. The gate voltage ranged from 0 to -80 V with a step size of -16 V was applied during the measurements. No obvious distortions were observed at the beginning of these out-put curves, indicating the good contacts between the gold electrodes and organic semiconductors.

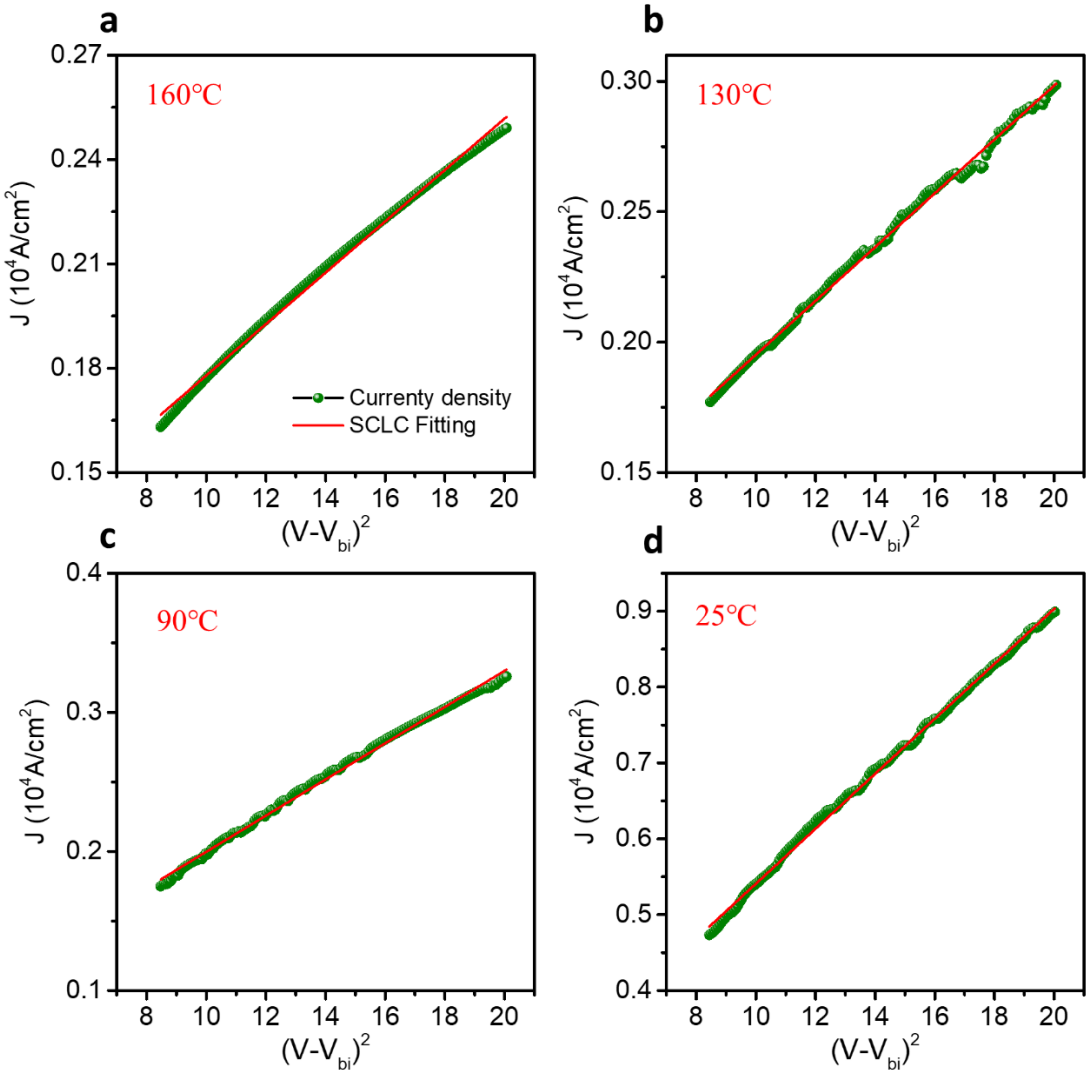

Figure S3. *J*-V characteristics measured by space-charge-limited current (SCLC) method. The intrinsic out-of-plane hole mobility of DPh-DNTT films fabricated at different substrate temperatures was achieved by fitting the *J*-*V* curve at the SCLC region. The configuration of the hole-only devices is ITO/NiO_x/DPh-DNTT/Au. The thickness of the DPh-DNTT film is fixed at 30 nm.

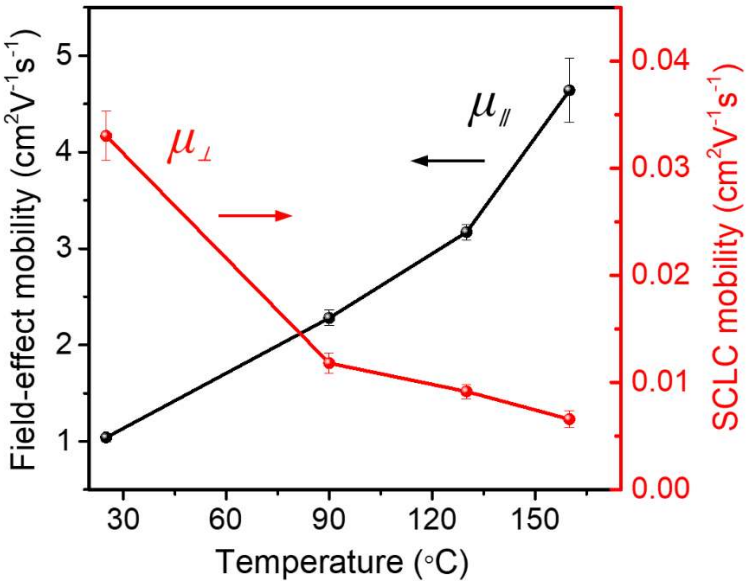

Figure S4. The in-plane and out-of-plane hole mobility of DPh-DNTT thin films evaporated at different substrate temperatures are extracted through the organic-field transistor (OFET) and SCLC measurements, respectively.

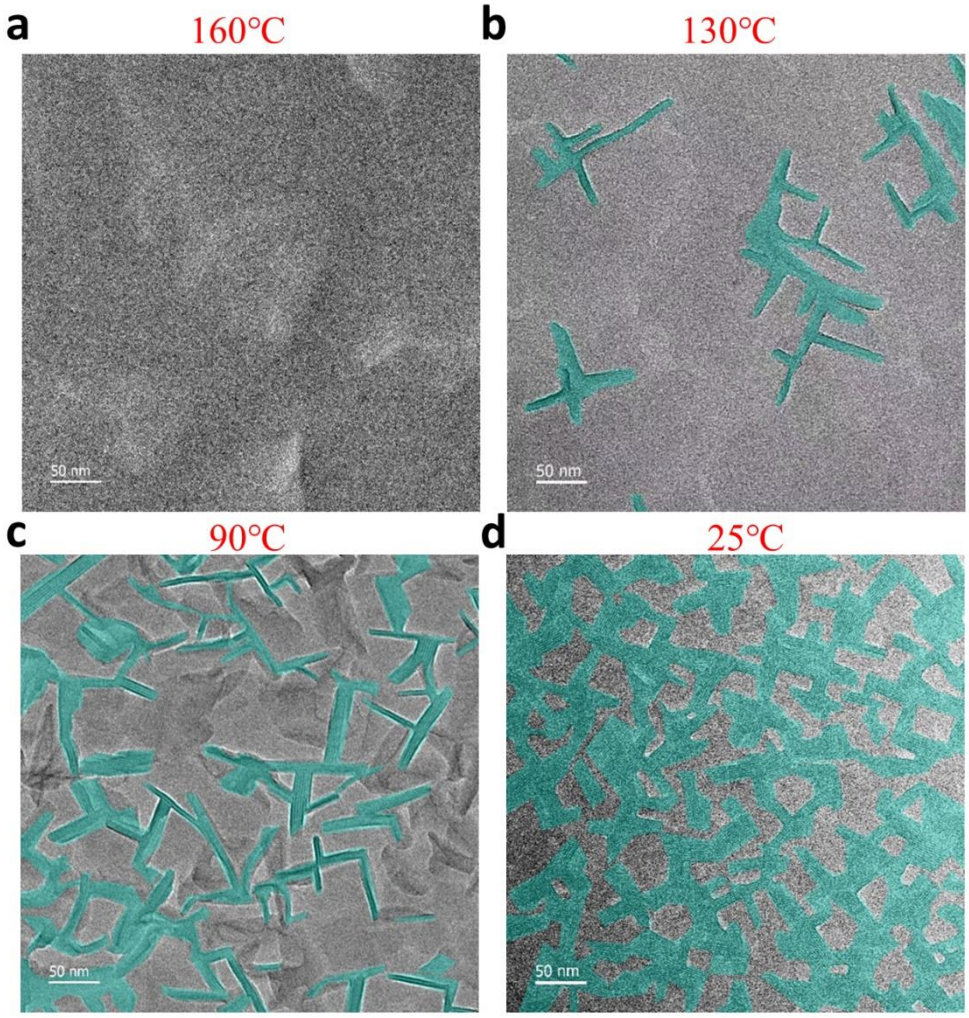

Figure S5. Top-view TEM images of DPh-DNTT films obtained at different substrate temperatures. The proportions of face-on molecular orientation within these DPh-DNTT films were roughly estimated to be none, 8.6%, 19.4%, and 59.6% at temperatures of 160, 130, 90, and 25°C, respectively.

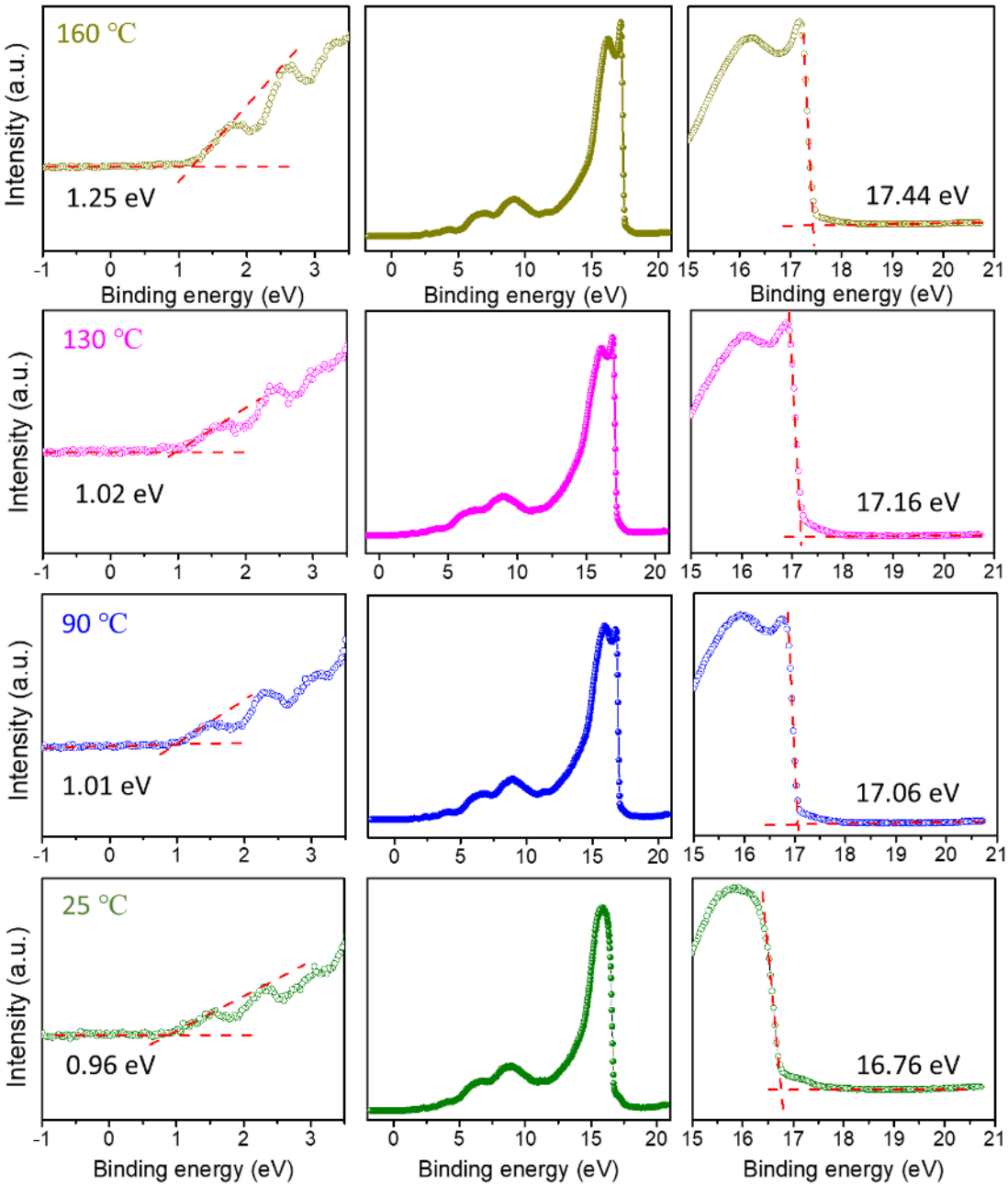

Figure S6. UPS results of the pristine DPh-DNTT films fabricated at different substrate temperatures.

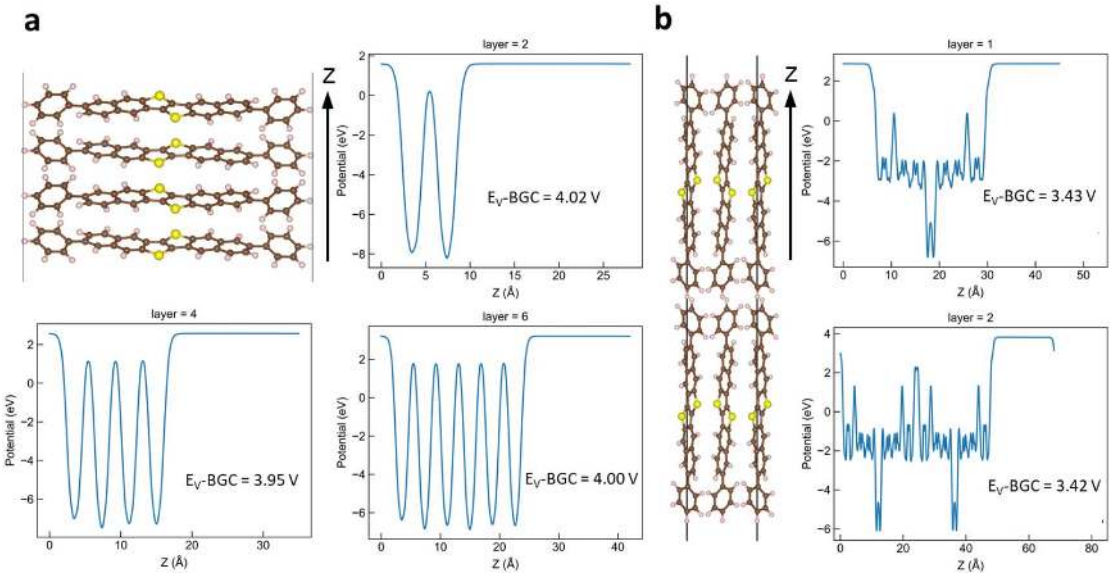

Figure S7. (a) Representative atomic structure for lying-down DPh-DNTT molecules with layer of 4 along with the electrostatic potential profiles perpendicular to the surface for systems with different layers (2, 4 and 6). (b) Representative atomic structure for standing-up DPh-DNTT molecules with layer of 2 along with electrostatic potentials perpendicular to the surface for systems with different layers (1 and 2). It is seen that calculations for different layers have almost same value for the difference between vacuum level (Ev) and band gap center (BGC).

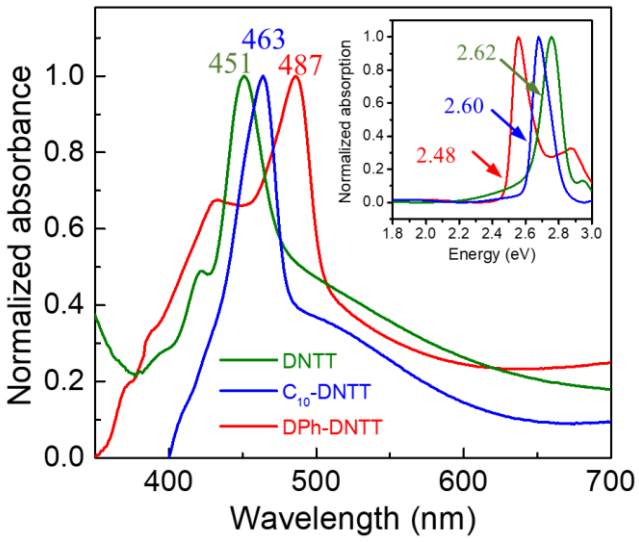

Figure S8. Normalized UV-Vis absorption spectra of thermally evaporated DNTT, C_{10}-DNTT and DPh-DNTT films ITO substrates at room temperature. The inset demonstrates their bandgaps calculated from the corresponding Tauc plots.

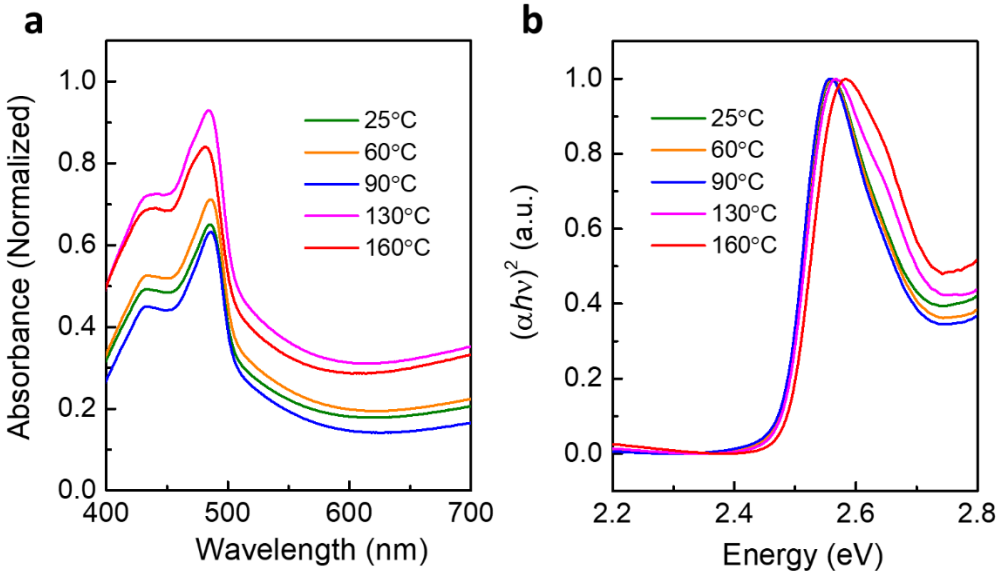

Figure S9. (a) UV-Vis absorption spectra of DPh-DNTT films fabricated under different temperatures and the corresponding Tauc plots (b).

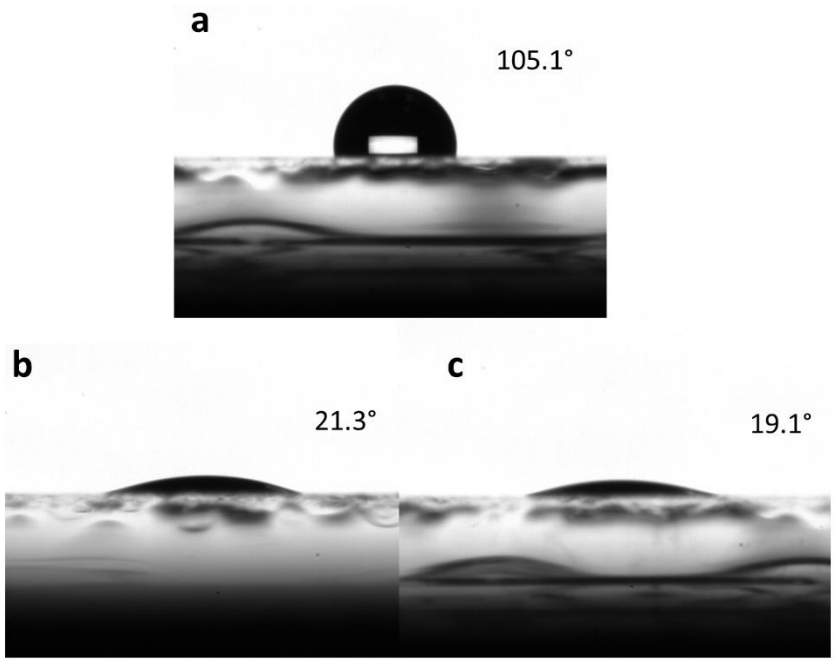

Figure S10. Contact angle measurements by dropping different solution on the surface of RT-DPh-DNTT film. (a) Deionized water. (b) N-N-dimethylformamide (DMF) solvent. (c) $MAPbI_3$-based perovskite solution.

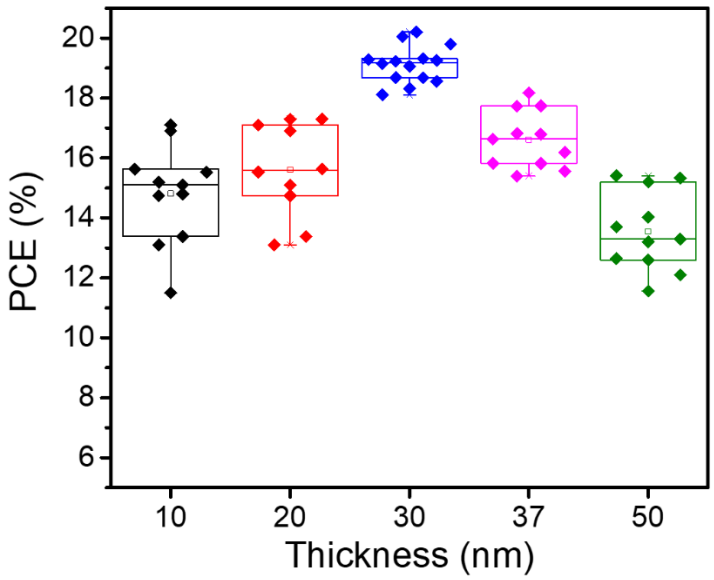

Figure S11. Optimizing the performance of RT-DPh-based perovskite solar cells by utilizing different thicknesses. The RT-DPh films were used as their pristine form.

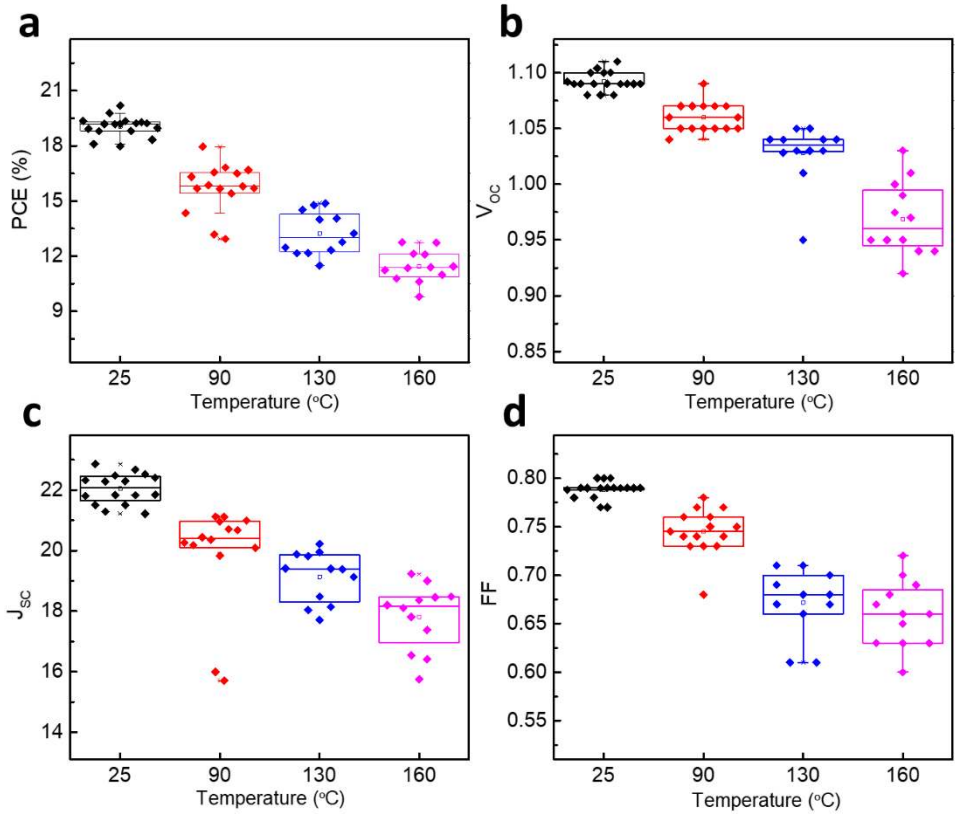

Figure S12. Photovoltaic performance of perovskite cells based on dopant-free DPh-DNTT films fabricated at different substrate temperatures.

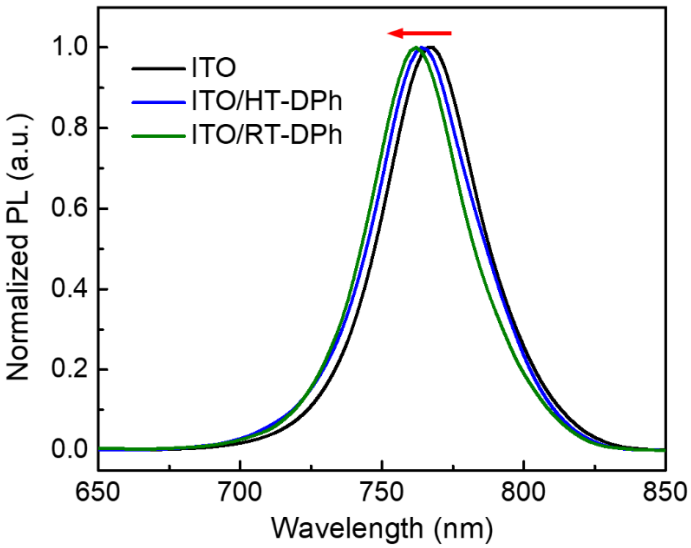

Figure S13. Normalized PL spectra of perovskite deposited on ITO, ITO/HT-DPh and ITO/RT-DPh substrates. The laser irradiated the samples from the ITO side.

Table S1. A summary of photovoltaic properties of $MAPbI_3$-based PSCs utilizing dopant-free organic semiconductors as HTMs.[6-42]

HTM	Device architecture	HOMO (eV)	Hole mobility ($cm^2m^{-1}s^{-1}$)	T_g (°C)	WCA* (°)	V_{oc} (V)	J_{sc} (mA cm^{-2})	FF (%)	Best PCE (%)	Ref.
TPA-TVT-TPA	p-i-n	-5.37	–	87	22.1	1.07	21.49	71	16.32	[6]
Trux-OMeTAD	p-i-n	-5.28	2.3×10^{-3}	212	90.4	1.02	23.20	79	18.60	[7]
NTPA	p-i-n	-5.27	1.1×10^{-3}	120	45.5	1.02	17.40	77	12.20	[8]
TPASB	p-i-n	-5.49	1.7×10^{-3}	–	–	1.05	20.80	80	17.60	[9]
TPAC3M	p-i-n	-4.96	1.1×10^{-5}	80	–	1.00	22.79	78	17.54	[10]
DFTAB	p-i-n	-5.20	2.4×10^{-5}	130		1.07	17.50	69	12.40	[11]
TPA-FLTPA-TPA	p-i-n	-5.45	–	162	–	1.05	20.82	78	17.10	[12]
BDT-POZ	p-i-n	-5.35	2.1×10^{-4}	–	89.9	1.04	22.56	81.7	19.16	[13]
TAPC	p-i-n	-5.50	3.6×10^{-3}	–	90.4	1.04	22.32	81.2	18.80	[14]
FMT	p-i-n	-4.89	2.0×10^{-6}	–	–	1.07	22.52	79.3	19.06	[15]
VB-MeO-FDPA	p-i-n	-5.18	3.0×10^{-4}	–	89.1	1.15	20.89	77.8	18.70	[16]
M118	p-i-n	-5.27	1.8×10^{-3}	112	92	1.06	22.40	72	17.10	[17]
XSln847	p-i-n	-5.26	7.8×10^{-5}	88	80.9	1.06	21.58	65.7	15.02	[18]
m-MTDATA	p-i-n	-5.10	2.4×10^{-5}	–	83	1.04	22.50	78	18.12	[19]
MC8-9-NPC	p-i-n	-5.51	–	–	102.6	0.90	20.80	74	13.85	[20]
V1036	p-i-n	-5.09	–	–	46.8	1.09	21.90	81	17.80	[21]
TFB	p-i-n	-5.40	3.0×10^{-3}	–	–	1.09	23.60	78.6	20.20	[22]
CuPrPC	n-i-p	-4.92	2.2×10^{-3}	–	106.6	1.01	23.2	76	17.80	[23]
mDPA-DBTP	n-i-p	-5.31	6.3×10^{-4}	–	96.4	1.12	21.13	76	18.09	[24]

PCA-1	n-i-p	-5.34	8.3×10^{-2}	–	–	1.02	20.81	73.2	15.59	[25]
TTE2	n-i-p	-5.30	6.2×10^{-4}	158	–	1.11	23.26	77.5	20.04	[26]
FBA3	n-i-p	-5.07	2.1×10^{-4}	78	–	1.09	22.12	79.9	19.27	[27]
IDTT-TPA	n-i-p	-5.00	6.6×10^{-4}	–	112.5	1.04	21.99	69.5	15.70	[28]
PPh-2MOD-PACZ	n-i-p	-5.22	9.1×10^{-5}	95	83.9	1.00	22.96	70	16.07	[29]
HTB-oMe	n-i-p	-5.33	5.5×10^{-4}	91	–	1.03	22.79	73.7	17.29	[30]
IDF-SFXPh	n-i-p	-5.22	1.4×10^{-4}	–	–	1.05	21.50	77.3	17.60	[31]
IDTC6-TPA	n-i-p	-5.13	4.3×10^{-4}	–	104.7	1.00	21.36	72.5	15.43	[32]
CuBuPc	n-i-p	-5.14	1.3×10^{-3}	–	106.8	1.02	21.00	70	15.00	[33]
CMO	n-i-p	-4.78	1.4×10^{-5}	–	92.5	0.93	25.19	67.9	15.92	[34]
PCA-1	mesoporous	-5.34	8.3×10^{-2}	–	–	1.06	22.30	76.7	18.17	[25]
NiPc-(oBu)8	mesoporous	-5.06	1.9×10^{-4}	–	–	1.08	23.10	73.4	18.30	[35]
Z1011	mesoporous	-5.21	8.5×10^{-4}	149	–	1.10	20.52	70	16.30	[36]
Ph-TPA-4A	mesoporous	-5.20	3.5×10^{-6}	173	88	1.05	23.29	72	18.03	[37]
Ph-TPA-6A	mesoporous	-5.18	7.5×10^{-4}		79.5	1.02	21.80	62	13.71	[37]
Z34	mesoporous	-5.14	7.5×10^{-4}	106	92.1	1.05	21.27	69	16.10	[38]
TPA-ANT-TPA	mesoporous	-5.32	2.6×10^{-4}	–	85	1.03	21.07	79.6	17.5	[39]
TPA-QA-TPA	mesoporous	-5.41	1.6×10^{-4}	–	–	0.99	22.4	75.1	16.6	[40]
ACE-QA-ACE	mesoporous	-5.59	2.3×10^{-4}	–	–	1.06	22.41	77	18.2	[40]
DPA-QA-DPA	mesoporous	-5.28	1.2×10^{-4}	74	–	0.95	22.38	73.2	15.50	[40]
CJ-01	mesoporous	-5.30	5.8×10^{-5}	92.1	82.8	1.11	22.32	74.7	18.56	[41]
ICTH2	mesoporous	-5.41	3.1×10^{-4}		92.8	1.03	24.78	73.5	18.75	[42]
DPh-DNTT	p-i-n	-5.42	3.1×10^{-2}	185	105.1	1.104	22.79	0.802	20.18	This work

* The WCA is the abbreviation of the water contact angle, indicating the wettability is characterized by water solvent.

Table S2. Fitted parameters of measured time-resolved PL (TRPL) spectra of perovskite films grown on ITO and ITO/DPh-DNTT substrates.

Sample	A_1 (%)	τ_1 (ns)	A_2 (%)	τ_2 (ns)	τ_{avg} (ns)*
ITO/perovskite	32.3	379.6	67.7	680.8	617.5
ITO/HT-DPh-DNTT/perovskite	43.3	222.3	56.7	307.9	277.5
ITO/RT-DPh-DNTT/perovskite	62.0	107.0	38.0	146.1	124.8

* τ_{avg} represents the averaged decay time that is calculated by the formula: $\tau_{avg} = (A_1\tau_1^2 + A_2\tau_2^2)/ (A_1\tau_1 + A_2\tau_2)$.

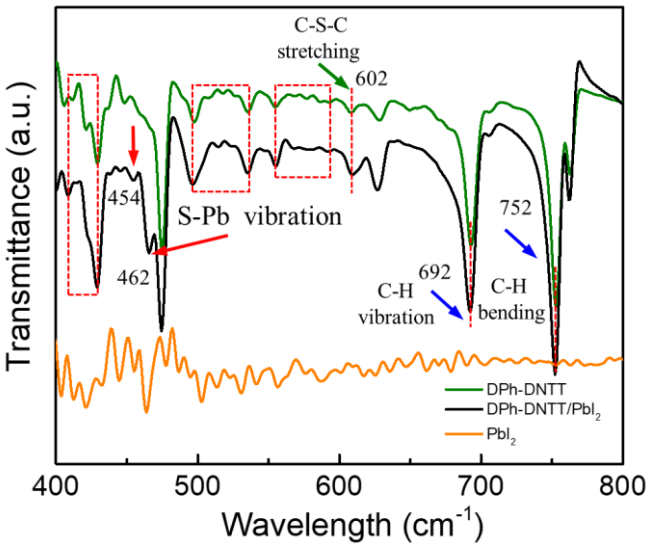

Figure S14. FTIR spectra of pure PbI_2, DPh-DNTT and DPh-DNTT blended with PbI_2. Compared with DPh-DNTT spectrum curve, there are two additional absorption peaks at 454 and 462 cm^{-1} that are assigned to the S-Pb interaction and several other variations are also observed which are pointed out by the dashed rectangle in the DPh-DNTT/PbI_2 profile.

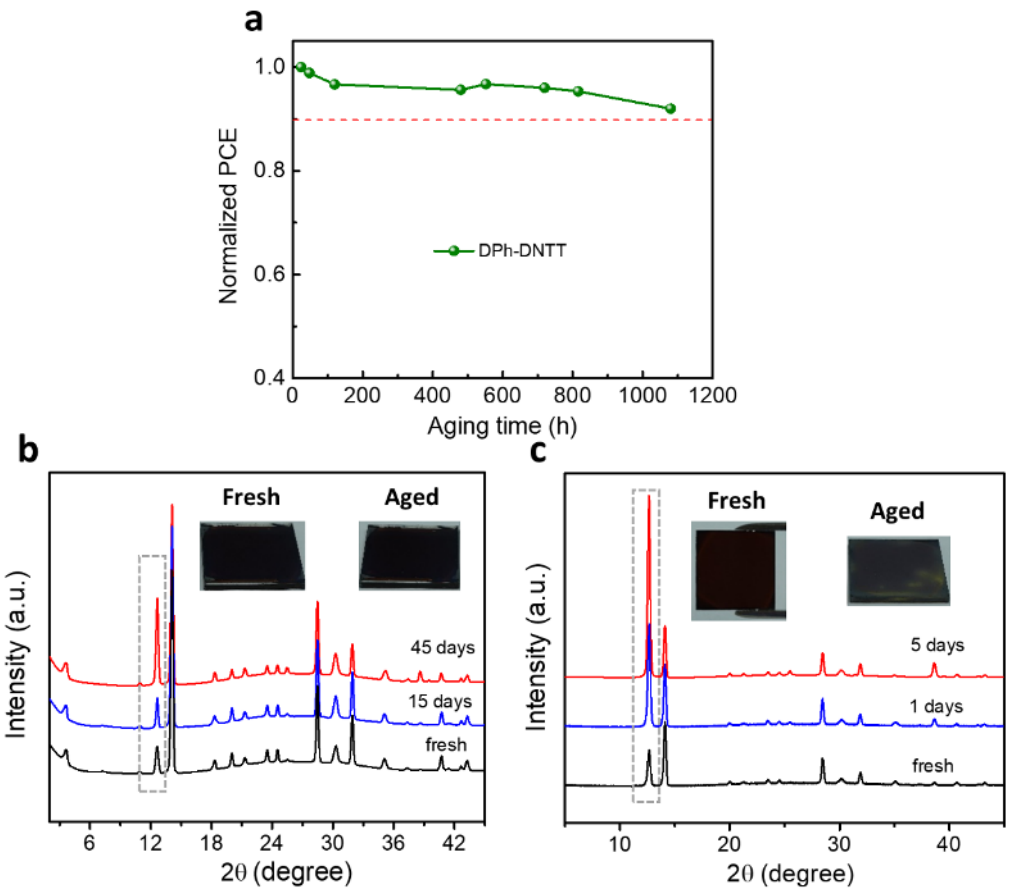

Figure S15. The air stability characterized by XRD technique. (a) Normalized PCE changes of RT-DPh-based perovskite solar cells stored at room temperature and a relative humidity (RH) of 60% ± 10% for different periods. (b) XRD patterns of RT-DPh/perovskite films after stored at the ambient environment with a RH of 60% ± 10% for different periods. (c) XRD patterns of ITO/perovskite films after storage under the same condition for several days. The insets are the optical photographs of the fresh and aged samples.

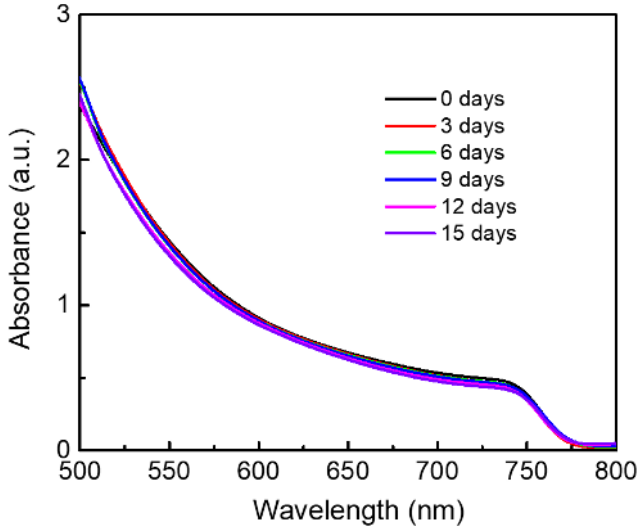

Figure S16. The thermal stability characterized by the UV-Vis spectroscopy. The encapsulated ITO/DPh-DNTT/$MAPbI_3$ films were treated at 85 ℃ in air for different days.

References

[1] P. E. Blöchl, Phys. Rev. B 1994, 50, 17953.

[2] G. Kresse, J. Furthmüller, Phys. Rev. B 1996, 54, 11169.

[3] J. Klimeš, D. R. Bowler, A. Michaelides, J. Phys. Condens. Matter 2009, 22, 022201.

[4] T. Leijtens, G. E. Eperon, N. K. Noel, S. N. Habisreutinger, A. Petrozza, H. J. Snaith, Adv. Energy Mater. 2015, 5, 1500963.

[5] M. C. Toroker, D. K. Kanan, N. Alidoust, L. Y. Isseroff, P. Liao, E. A. Carter, Phys. Chem. Chem. Phys. 2011, 13, 16644.

[6] H. D. Pham, H. Hu, K. Feron, S. Manzhos, H. Wang, Y. M. Lam, P. Sonar, Solar RRL 2017, 1, 1700105.

[7] C. Huang, W. Fu, C.-Z. Li, Z. Zhang, W. Qiu, M. Shi, P. Heremans, A. K.-Y. Jen, H. Chen, J. Am. Chem. Soc. 2016, 138, 2528.

[8] M. Neophytou, J. Griffiths, J. Fraser, M. Kirkus, H. Chen, C. B. Nielsen, I. McCulloch, J. Mater. Chem. C 2017, 5, 4940.

[9] Y. Li, Z. Xu, S. Zhao, B. Qiao, D. Huang, L. Zhao, J. Zhao, P. Wang, Y. Zhu, X. Li, Small 2016, 12, 4902.

[10] S. J. Park, S. Jeon, I. K. Lee, J. Zhang, H. Jeong, J.-Y. Park, J. Bang, T. K. Ahn, H.-W. Shin, B.-G. Kim, J. Mater. Chem. A 2017, 5, 13220.

[11] A. E. Labban, H. Chen, M. Kirkus, J. Barbe, S. Del Gobbo, M. Neophytou, I. McCulloch, J. Eid, Adv. Energy Mater. 2016, 6, 1502101.

[12] H. D. Pham, L. Gil-Escrig, K. Feron, S. Manzhos, S. Albrecht, H. J. Bolink, P. Sonar, J. Mater. Chem. A 2019, 7, 12507.

[13] Y. Chen, X. Xu, N. Cai, S. Qian, R. Luo, Y. Huo, S. W. Tsang, Adv. Energy Mater. 2019, 9, 1901268.

[14]L. Yang, F. Cai, Y. Yan, J. Li, D. Liu, A. J. Pearson, T. Wang, Adv. Funct. Mater. 2017, 27, 1702613.

[15]J. Zhang, Q. Sun, Q. Chen, Y. Wang, Y. Zhou, B. Song, N. Yuan, J. Ding, Y. Li, Adv. Funct. Mater. 2019, 29, 1900484.

[16]Y. Zhang, C. Kou, J. Zhang, Y. Liu, W. Li, Z. Bo, M. Shao, J. Mater. Chem. A 2019, 7, 5522.

[17]B. Wang, Q. Zeng, Z. Sun, S. Xue, M. Liang, Dyes Pigm. 2019, 165, 81.

[18]N. Liu, X. Zong, Z. Wang, T. Cui, M. Liang, Y. Zhang, S. Xue, Electrochim. Acta 2019, 296, 283.

[19]R. Chen, T. Bu, J. Li, W. Li, P. Zhou, X. Liu, Z. Ku, J. Zhong, Y. Peng, F. Huang, ChemSusChem 2018, 11, 1467.

[20]L. Bai, Z. Wang, Y. Han, Z. Zuo, B. Liu, M. Yu, H. Zhang, J. Lin, Y. Xia, C. Yin, Nano Energy 2018, 46, 241.

[21]A. Magomedov, A. Al-Ashouri, E. Kasparavičius, S. Strazdaite, G. Niaura, M. Jošt, T. Malinauskas, S. Albrecht, V. Getautis, Adv. Energy Mater. 2018, 8, 1801892.

[22]D. Yang, T. Sano, Y. Yaguchi, H. Sun, H. Sasabe, J. Kido, Adv. Funct. Mater. 2019, 29, 1807556.

[23]X. Liu, Y. Wang, E. Rezaee, Q. Chen, Y. Feng, X. Sun, L. Dong, Q. Hu, C. Li, Z. X. Xu, Solar RRL 2018, 2, 1800050.

[24]R. Azmi, S. Y. Nam, S. Sinaga, Z. A. Akbar, C.-L. Lee, S. C. Yoon, I. H. Jung, S.-Y. Jang, Nano Energy 2018, 44, 191.

[25]Y. Li, K. R. Scheel, R. G. Clevenger, W. Shou, H. Pan, K. V. Kilway, Z. Peng, Adv. Energy Mater. 2018, 8, 1801248.

[26]C. Shen, Y. Wu, H. Zhang, E. Li, W. Zhang, X. Xu, W. Wu, H. Tian, W. H. Zhu, Angew. Chem. Int. Ed. 2019, 58, 3784.

[27]X. Sun, F. Wu, C. Zhong, L. Zhu, Chem. Sci. 2019, 10, 6899.

[28]X. Liu, X. Zheng, Y. Wang, Z. Chen, F. Yao, Q. Zhang, G. Fang, Z. K. Chen, W. Huang, Z. X. Xu, ChemSusChem 2017, 10, 2833.

[29]W. Yu, Q. Yang, J. Zhang, D. Tu, X. Wang, X. Liu, G. Li, X. Guo, C. Li, ACS Appl. Mater. Interfaces 2019, 11, 30065.

[30]B.-B. Cui, Y. Han, N. Yang, S. Yang, L. Zhang, Y. Wang, Y. Jia, L. Zhao, Y.-W. Zhong, Q. Chen, ACS Appl. Electron. Mater. 2018, 10, 41592.

[31]F. Liu, F. Wu, Z. Tu, Q. Liao, Y. Gong, L. Zhu, Q. Li, Z. Li, Adv. Funct. Mater. 2019, 29, 1901296.

[32]X. Liu, E. Rezaee, H. Shan, J. Xu, Y. Zhang, Y. Feng, J. Dai, Z.-K. Chen, W. Huang, Z.-X. Xu, J. Mater. Chem. C 2018, 6, 4706.

[33]Y. Feng, Q. Chen, L. Dong, Z. Zhang, C. Li, S. Yang, S. Cai, Z.-X. Xu, Sol. Energy 2019, 184, 649.

[34]J. Zhang, L. Xu, P. Huang, Y. Zhou, Y. Zhu, N. Yuan, J. Ding, Z. Zhang, Y. Li, J. Mater. Chem. C 2017, 5, 12752.

[35]M. Cheng, Y. Li, M. Safdari, C. Chen, P. Liu, L. Kloo, L. Sun, Adv. Energy Mater. 2017, 7, 1602556.

[36]F. Zhang, C. Yi, P. Wei, X. Bi, J. Luo, G. Jacopin, S. Wang, X. Li, Y. Xiao, S. M. Zakeeruddin, Adv. Energy Mater. 2016, 6, 1600401.

[37]J.-Y. Feng, K.-W. Lai, Y.-S. Shiue, A. Singh, C. P. Kumar, C.-T. Li, W.-T. Wu, J. T. Lin, C.-W. Chu, C.-C. Chang, J. Mater. Chem. A 2019, 7, 14209.

[38]F. Zhang, X. Liu, C. Yi, D. Bi, J. Luo, S. Wang, X. Li, Y. Xiao, S. M. Zakeeruddin, M. Grätzel, ChemSusChem 2016, 9, 2578.

[39]H. D. Pham, T. T. Do, J. Kim, C. Charbonneau, S. Manzhos, K. Feron, W. C. Tsoi, J. R. Durrant, S. M. Jain, P. Sonar, Adv. Energy Mater. 2018, 8, 1703007.

[40]H. D. Pham, S. M. Jain, M. Li, S. Manzhos, K. Feron, S. Pitchaimuthu, Z. Liu, N. Motta, H. Wang, J. R. Durrant, J. Mater. Chem. A 2019, 7, 5315.

[41]J. Chen, J. Xia, H.-J. Yu, J.-X. Zhong, X.-K. Wu, Y.-S. Qin, C. Jia, Z. She, D.-B. Kuang, G. Shao, Chem. Mater. 2019, 31, 5431.

[42]D. Bharath, M. Sasikumar, N. R. Chereddy, J. R. Vaidya, S. Pola, Sol. Energy 2018, 174, 130.